

1 Radiometric validation of atmospheric correction for MERIS in the Baltic Sea  
2 based on continuous observations from ships and AERONET-OC

3  
4 Ping Qin<sup>a,b</sup>, Stefan G.H. Simis<sup>a</sup>, Gavin H. Tilstone<sup>a,\*</sup>

5  
6 <sup>a</sup> Plymouth Marine Laboratory, Prospect Place, The Hoe, Plymouth PL1 3DH, UK

7 <sup>b</sup> College of Information Science and Engineering, Ocean University of China, Qingdao 266100, China

8  
9  
10  
11 \*Corresponding author: [ghti@pml.ac.uk](mailto:ghti@pml.ac.uk)

12  
13 Running head: Atmospheric correction models for MERIS in the Baltic Sea

14  
15 Keywords: Atmospheric Correction, Baltic Sea, Remote Sensing Reflectance, MERIS, AERONET-OC,  
16 Shipborne radiometry.

## 18 ABSTRACT

19 The Baltic Sea is a semi-enclosed sea that is optically dominated by coloured dissolved organic material  
20 (CDOM) and has relatively low sun elevation which makes accurate ocean colour remote sensing challenging  
21 in these waters. The high absorption, low scattering properties of the Baltic Sea are representative of other  
22 optically similar water bodies including the Arctic Ocean, Yellow Sea, Black Sea, coastal regions adjacent to  
23 the CDOM-rich estuaries such as the Amazon, and highly absorbing lakes where radiometric validation is  
24 essential in order to develop accurate remote sensing algorithms. Previous studies in this region mainly  
25 focused on the validation and improvement of standard Chlorophyll-a (Chl *a*) and attenuation coefficient ( $k_d$ )  
26 ocean colour products. The primary input to derive these is the water-leaving radiance ( $L_w$ ) or remote sensing  
27 reflectance ( $R_{rs}$ ) and it is therefore fundamental to obtain the most accurate  $L_w$  or  $R_{rs}$  before deriving higher  
28 level products. To this end, the retrieval accuracy of  $R_{rs}$  from Medium Resolution Imaging Spectrometer  
29 (MERIS) imagery using six atmospheric correction processors was assessed through above-water  
30 measurements at two sites of the Aerosol Robotic Network for Ocean Colour (AERONET-OC; 363  
31 measurements) and a shipborne autonomous platform from which the highest number of measurements were  
32 obtained (4986 measurements). The six processors tested were the CoastColour processor (CC), the Case 2  
33 Regional processor for lakes (C2R-Lakes), the Case 2 Regional CoastColour processor (C2R-CC), the  
34 FUB/WeW water processor (FUB), the MERIS ground segment processor (MEGS) and POLYMER. All  
35 processors except for CC had small average absolute percentage differences ( $\psi$ ) in the wavelength range from  
36 490 nm to 709 nm ( $\psi < 40\%$ ), while other bands had larger differences with  $\psi > 60\%$ . Compared to *in situ*  
37 values, the  $R_{rs}(709)/R_{rs}(665)$  band ratio had  $\psi < 30\%$  for all processors. The most accurate  $R_{rs}$  in the 490 to  
38 709 nm domain was obtained from POLYMER with  $\psi < 30\%$  and coefficients of determination ( $R^2$ )  $> 0.6$ .  
39 Using a score system based on all statistical tests, POLYMER scored highest, while C2R-CC, C2R-Lakes and  
40 FUB had lower scores. This study represents the largest data base of *in situ*  $R_{rs}$ , the most comprehensive  
41 analysis of AC models for highly absorbing waters and for MERIS, conducted to date. The results have  
42 implications for the new generation of Copernicus Sentinel ocean colour satellites.

43

44

## 45 1 Introduction

46 Remote sensing has become an important tool to monitor the dynamics of optically active substances in the  
47 marine environment due to high coverage at both spatial and temporal scales (IOCCG, 2000). Some

48 bio-optical and geophysical variables, such as the concentration of chlorophyll *a* (Chl *a*) as an indicator of  
49 phytoplankton biomass, suspended particulate matter, coloured dissolved organic matter (CDOM), as well as  
50 the bulk inherent optical properties of the visible surface layer, have been successfully retrieved from  
51 water-leaving radiance ( $L_w$ ) or remote sensing reflectance ( $R_{rs}$ ).  $L_w$  or  $R_{rs}$  at the sea surface is derived from the  
52 top-of-atmosphere (TOA) radiance after atmospheric correction (AC). In principle, the more accurate  $L_w$  or  $R_{rs}$ ,  
53 the more accurate will be the derived biogeochemical products. The performance of atmospheric correction is  
54 therefore key to quality assured ocean colour data for monitoring issues of water quality, carbon cycling and  
55 climate change.

56 Various AC methods have been developed for remote sensing of the open-ocean, coastal seas, and inland  
57 waters. In the open ocean, AC mainly rely on the black pixel hypothesis (Gordon and Wang 1994) which  
58 assumes that the marine reflectance in the near infrared (NIR, 700–1000 nm) is negligible due to the relatively  
59 high absorption of water itself. The TOA radiance in the NIR wavebands is further influenced by absorption  
60 and scattering from atmospheric aerosols, and the reflectance in the short visible domain (400–700 nm) is  
61 extrapolated through spectral aerosol models. The black pixel assumption is too simplistic for most inland and  
62 coastal waters since the contributions to  $R_{rs}$  of suspended particulates can cause  $R_{rs}$  in the near-infrared  
63 wavelength range to depart from zero (Ruddick *et al.*, 2000; Hu *et al.*, 2000; Knaeps *et al.*, 2012). Alternative  
64 AC methods have been proposed to cope with a variety of the Case 2 waters, including the black pixel method  
65 by means of the short wave infrared or ultraviolet wavebands (Wang & Shi, 2007; Siegel *et al.*, 2000; He *et al.*,  
66 2012), spectral optimization that utilizes a bio-optical model in conjunction with radiative transfer models  
67 (Steinmetz *et al.*, 2011; Callieco & Dell'Acqua, 2011), and artificial neural networks (Schiller & Doerffer,  
68 1999; Doerffer, 2007; Schroeder *et al.*, 2007; Brockmann *et al.*, 2016).

69 MERIS on the European Space Agency ENVISAT mission, during its operation in 2002–2012, offered a  
70 wide dynamic range of products for both marine and terrestrial observations. It provided global coverage in 3  
71 days, with observations at 15 bands at visible and NIR wavelengths designed to observe both open-ocean and  
72 coastal environments. It also provided data at full (~ 300 m) and reduced (~ 1200 m) resolution. The MERIS  
73 era marked the start of long-term remote sensing observations of water quality in optically complex  
74 environments. A range of atmospheric correction processors were developed for MERIS, designed for a wide  
75 range of applications from coastal to inland waters. These include the CoastColour (CC) processor (Doerffer  
76 and Schiller, 2007), the Case 2 Regional (C2R) processor (Doerffer and Schiller, 2008), the FUB/WeW water  
77 (FUB) processor (Schroeder *et al.*, 2007), and the Case 2 Regional CoastColour (C2R-CC) processor

78 (Brockmann *et al.*, 2016). In addition, the default MERIS ground segment (MEGS) processor has been  
79 continually updated (Aiken & Moore, 2000) to reflect the performance of the MERIS instrument over its  
80 lifespan. An alternative polynomial based algorithm (POLYMER) (Steinmetz *et al.*, 2011) has been  
81 increasingly used with MERIS and other sensors, though it was not the primary choice for optically complex  
82 waters.

83 The high-CDOM waters of the Baltic Sea are characteristic of water bodies with high riverine input, long  
84 water retention times, but low mineral particle loading, such as the Arctic Ocean, Yellow Sea, Black Sea,  
85 coastal regions adjacent to the CDOM-rich estuaries such as the Amazon, and highly absorbing lakes. In these  
86 environments, reflectance at short visible wavelengths is particularly low and may contribute as little as 0.4%  
87 of the TOA radiance, compared to 9.8% over open ocean waters (IOCCG, 2010). The performance of AC  
88 processors dedicated to high absorbing coastal waters, have thus far not been as successful as those applied to  
89 turbid waters which have a stronger reflectance signal. Regional re-tuning of some AC processors has  
90 improved their performance in some highly absorbing waters (Attila *et al.*, 2013).

91 Previous research in the Baltic Sea evaluated the performance of standard and Case 2-specific Chl *a*  
92 (Harvey *et al.* 2015; D'Alimonte *et al.* 2012; Kratzer *et al.* 2008; Melin *et al.* 2007; Reinart and Kutser 2006)  
93 and  $k_d$  (Stramska and Swirgon 2014; Doron *et al.* 2011; Pierson *et al.* 2008) ocean colour products. Regionally  
94 calibrated blue-green ratio versions of OC4v6 (Pitarch *et al.*, 2016; Darecki and Stramski, 2004) have allegedly  
95 improved the accuracy of Chl *a* retrieval in the Baltic Sea, but do not work for waters where CDOM dominates  
96 the absorption in the blue. Using longer wavelengths such as red-to-green (Wozniak 2014) and  
97 red-to-near-infra red (Koponen *et al.* 2007; Krawczyk *et al.* 1997, Matthews 2011) is therefore advisable in  
98 these optically complex, CDOM-rich waters. Ligi *et al.* (2016) assessed 30 empirical remote sensing  
99 algorithms for retrieving Chl *a* in the Baltic Sea through modelled and *in situ* reflectance data, and found that  
100 NIR-red band ratio algorithms performed best. Few papers have considered the performance of and improving  
101 the accuracy of the primary input,  $L_w$  or  $R_{rs}$ , of SeaWiFS, MODIS-Aqua and MERIS, used to derive Chl *a* and  
102  $k_d$  products (D'Alimonte *et al.* 2014; Zibordi *et al.* 2009; Kratzer *et al.* 2008; Melin *et al.* 2007; Darecki &  
103 Stramski 2004; Ohde *et al.* 2002). Some studies have improved the performance of regional specific Chl *a*  
104 algorithms for the Baltic Sea using FUB and C2R processors coupled to AC neural networks has been  
105 improved (Beltrán-Abaunza *et al.*, 2014; Attila *et al.* 2013; Kratzer *et al.* 2008). Melin *et al.* (2013) and  
106 Bulgarelli *et al.* (2003) also showed that improvements in the aerosol libraries used in the AC processors for  
107 MERIS and SeaWiFS also improves retrieval of  $R_{rs}$ . Some studies have shown that the accuracy of both the

108 shape and amplitude of  $L_w$  or  $R_{rs}$  are required otherwise improvements in green to near infrared bands but  
109 failure in the blue bands may result in reasonable Chl  $a$  concentration retrieval but a failure in the retrieval of  
110 other products, such as absorption by CDOM.

111 Another common challenge to achieve this is obtaining sufficient in situ data to carry out a comprehensive  
112 analysis of satellite  $R_{rs}$ . Both MOBY (Voss et al. 2007), BOUSOLLE (Antoine et al. 2008) and  
113 AERONET-OC (Zibordi, *et al*, 2009b) have undoubtedly aided the global assessment of ocean colour products.  
114 These platforms are fixed structures, close to the coast, and though temporal coverage from them is good,  
115 spatial coverage is limited. A growing network of autonomous radiometers deployed on research ships and  
116 ships of opportunity such as ferries could potentially fill these spatial gaps in data coverage, provided that the  
117 same high quality measurements on shipborne platforms are achieved as on the fixed platforms. To this end in  
118 this paper, by combining shipborne and AERONET-OC measurements, and using a rigorous quality control  
119 procedure for the ship data (Simis and Olsson 2013), we use the use the largest data base to date of in situ  $R_{rs}$   
120 to evaluate the performance, accuracy and suitability of six AC processors for MERIS for the Baltic Sea. The  
121 retrieval accuracy at each band and spectral shape of CC, C2R, C2R-CC, FUB, MEGS and POLYMER  
122 processors were evaluated against *in situ*  $R_{rs}$  from two AERONET-OC measurement platforms and a prototype  
123 platform for continuous shipborne reflectance measurements operated from a research vessel, which has since  
124 been installed on two merchant vessels on the Alg@line network managed by the Finnish Environment  
125 Institute (SYKE).. The suitability of each processor at different locations as well as the seasonal bias in  
126 retrieval of  $R_{rs}$ , was also compared.

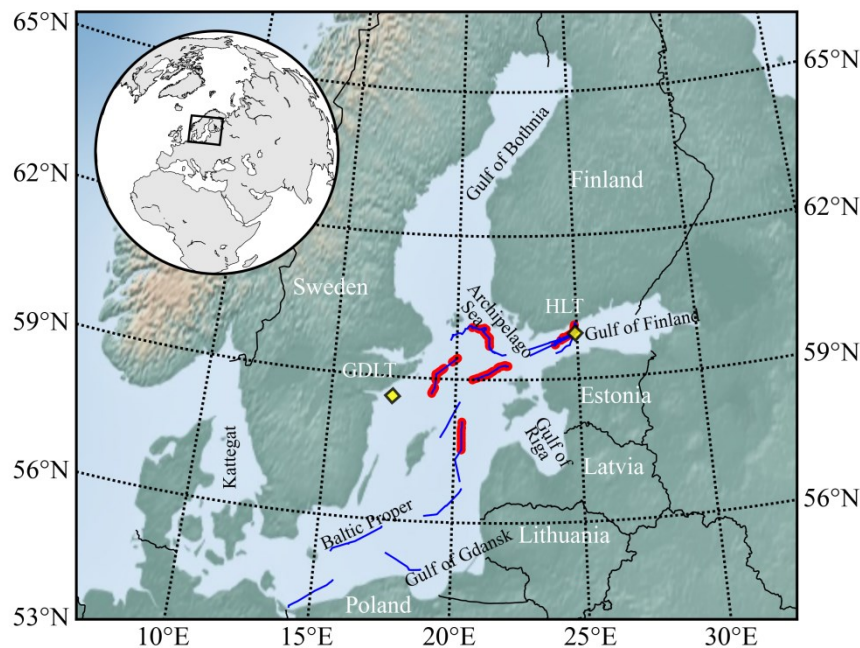
127

## 128 **2 Data and Methods**

### 129 *2.1 Study area*

130 The Baltic Sea is a semi-enclosed brackish marine water body located in Northern Europe between the  
131 maritime temperate and continental sub-Arctic zones (Fig. 1), and has partial, seasonal sea-ice cover. It covers  
132 an area of  $\sim 400\,000$  km<sup>2</sup> which includes the Gulf of Bothnia, Gulf of Finland, Gulf of Riga, Gulf of Gdansk  
133 and Kattegat Bay. The mean water depth over the region is approximately 54 m and tides are negligible due to  
134 limited connectivity with the Atlantic Ocean. One of the main characteristics of the Baltic Sea is the salinity  
135 gradient that increases from the north with salinity  $< 1$  PSU to the south-west with salinity up to  $> 20$  PSU.  
136 Riverine input is large and seasonal, with annual mean river runoff of  $\sim 14000$  m<sup>3</sup>/s (Leppäranta & Myrberg,  
137 2009; Omstedt *et al.*, 2004). Eutrophication and pollution are significant in the region due to the terrestrial

138 input of nitrogen and phosphorus and the limited water exchange with the North Sea.



139  
140 **Fig. 1.** Locations of *in situ* data from the research vessel (RV, blue lines) and two AERONET-OC sites (yellow markers): Gustaf  
141 Dalen Lighthouse Tower (GDLT) and Helsinki Lighthouse Tower (HLT). Red markers represent match-ups with the shipborne  
142 observations.

143

144 CDOM absorption coefficients at 440 nm are generally  $> 1.0 \text{ m}^{-1}$ , with higher values in estuaries and bays,  
145 such as the Neva Bay where  $a_{\text{CDOM}}(442)$  is  $3.77 \text{ m}^{-1}$  (Wozniak *et al.*, 2014; Ylöstalo *et al.*, 2016). There are  
146 generally two annual phytoplankton blooms in the Baltic Sea. The spring bloom is dominated by diatoms and  
147 dinoflagellates, and exhibits high peak biomass but this is generally short-lived from March to April. The  
148 summer bloom is dominated by cyanobacteria from July to September, when there is thermal stratification and  
149 cyanobacteria accumulate during prolonged calm weather (Kahru *et al.* 2015; Groetsch *et al.*, 2014).

150

## 151 2.2 Shipborne observations

152 *In situ* radiometric observations from the shipborne platform were acquired during three cruises on R/V  
153 Aranda in the Baltic Sea during spring (April) 2011 and summer (July) 2010 and 2011 in the Gulf of Finland,  
154 the Baltic Proper and the Archipelago Sea (Fig. 1).

155 Three RAMSES spectro-radiometers (TriOS Optical Sensors, Rastede, Germany) were mounted on the  
156 bow of the research vessel. A RAMSES-ACC with cosine collector optics was directed upwards to record the

157 downwelling irradiance above the water surface ( $E_d$ ), and two RAMSES-ARC radiance sensors were used to  
 158 measure the sky radiance ( $L_s$ ) and the total upwelling radiance pointed at the surface of the water ( $L_t$ ), at 140°  
 159 and 40° zenith angles respectively. The azimuth angle in relation to the solar azimuth was kept as close to 135°  
 160 as possible using a stepper motor platform to compensate for the solar azimuth (calculated from GPS time and  
 161 location) and vessel heading, without pointing back at the ship, and was always  $> 90^\circ$  (Simis & Olsson, 2013).  
 162 Three sensors recorded the wavelength range of 320–950 nm with 3.3 nm spectral resolution and a  
 163 field-of-view of 7° at 15-s intervals. Inter-calibration of the sensors was verified before each cruise by pointing  
 164 the radiance sensors at a large white spectralon panel and simultaneously recording  $E_d$  on the roof of the  
 165 laboratory on a day with clear skies.  $R_{rs}$  ( $\text{sr}^{-1}$ ) was then calculated as follows:

$$R_{rs}(\lambda) = L_{w+}(\lambda) / E_d(\lambda) \quad (1)$$

$$L_{w+}(\lambda) = L_t(\lambda) - \rho_s L_s(\lambda) \quad (2)$$

166 where  $L_{w+}$  is the water-leaving radiance just above the sea surface and  $\rho_s$  is the reflectance of sky radiance at  
 167 the air-water interface, which depends on solar azimuth angle, viewing geometry, wind speed, cloud and  
 168 surface roughness (Mobley, 1999; Ruddick *et al.*, 2006; Mobley, 2015). Here  $\rho_s$  was determined using the  
 169 fingerprint method (Simis & Olsson, 2013), a spectral optimization technique that minimizes the propagation  
 170 of atmospheric absorption features to  $R_{rs}$  and flag observations that do not resolve to a smooth  $R_{rs}$  spectrum.

171 The shipborne reflectance underwent a secondary screening procedure to eliminate spurious observations  
 172 based on assumptions of the spectral shapes of reflectance in the highly absorbing and weakly scattering  
 173 waters of the Baltic Sea. The following threshold criteria were used: (1) the average  $R_{rs}$  in the ultraviolet range  
 174 (350–400 nm) and near infra-red (800–900 nm) should not be significantly negative, i.e.  $R_{rs}(350-400) \geq$   
 175  $-0.0005 \text{ sr}^{-1}$  and  $R_{rs}(800-900) \geq -0.0005 \text{ sr}^{-1}$ . (2) The maximum reflectance value was limited to  $R_{rs}(\lambda) < 0.015$   
 176  $\text{sr}^{-1}$ , which removed spectra strongly affected by sun glint, whitecaps, or spray. (3) Spectra were only  
 177 considered valid if they retained a green reflectance peak, following the criterion  $1.5R_{rs}(400) < R_{rs}(580) >$   
 178  $2R_{rs}(800)$ . This shape of the spectrum is expected in CDOM-rich waters with minor contribution to scattering  
 179 from mineral particles, such that CDOM and pure water absorption dominate the blue and near infra-red  
 180 reflectance, respectively. (4) Following the same assumption, CDOM absorption increases towards shorter  
 181 wavelengths, spectra were validated with the criterion  $R_{rs}(412) < R_{rs}(443)$ , which removed spectra affected by  
 182 incomplete removal of reflected sky light causing a rise of reflectance in the blue. (5) Removal of spectra  
 183 where the difference between the maximum and minimum  $R_{rs}$  in the 760–770 nm wavelengths was larger than

184 10% of the maximum  $R_{rs}(560-600)$ , i.e. clearly showing an effect of the oxygen absorption peak. This set of  
185 filtering criteria applies specifically to conditions in the Baltic Sea and should be revised for other water bodies.  
186 Shipborne collection of  $R_{rs}(\lambda)$  should be significantly less challenging in more turbid coastal waters with a  
187 higher amplitude of reflectance and lower errors associated with the removal of reflected sky radiance.  
188 Following this screening procedure, the  $R_{rs}(\lambda)$  spectra are given in Figure 2.

189 The NIR reflectance is expected to be close to zero in waters with low particle scattering (Hooker *et al.*,  
190 2002). The NIR reflectance measured in the Baltic Sea may depart significantly from zero near to river plumes  
191 or when there is an accumulation of near-surface phytoplankton. In most cases, however, an offset from zero in  
192 the NIR will be primarily attributed to residual surface water effects (spray, sun glint, whitecaps, and sky  
193 radiance including scattered cloud reflected on waves). Removal of the offset in the NIR reflectance minimizes  
194 additional contamination in the signal and leads to a better correlation with the satellite signal. The fingerprint  
195 method to resolve  $R_{rs}(\lambda)$  per definition accounts for direct and diffuse contributions to sky radiance reflected at  
196 the water surface. Any offset observed in the NIR that is not due to high particle scatter is expected to be  
197 spectrally neutral and can be compensated for, by subtracting this signal from the  $R_{rs}(\lambda)$ . In theory, the validity  
198 of this assumption can be easily checked by evaluating the shape of the NIR signal. For high particle scattering,  
199 this shape should reflect the spectral dependence of water absorption. When this is not the case, high particle  
200 scattering cannot account for the NIR offset and may thus be subtracted. The shape of the NIR signal did not  
201 generally show a spectral dependence of water absorption in the Baltic Sea (results not shown). NIR  
202 offset-corrected  $R_{rs}(\lambda)$  is here defined as  $R_{rs}(\lambda)$  from which the average  $R_{rs}$  in the near infrared region (850–  
203 900 nm) is subtracted. The difference between performing and not performing offset correction was compared  
204 (Table 3).

205

### 206 2.3 AERONET-OC

207 AERONET-OC is a standardized measurement system installed on fixed platforms at a range of coastal  
208 locations to collect marine radiometric measurements coincident with aerosol measurements for retrieving  
209 aerosol optical properties (Zibordi *et al.*, 2009b). Measurements from two AERONET-OC sites were used from  
210 April 2005 to October 2011: the Gustaf Dalén Lighthouse Tower (GDLT) in the northern Baltic Proper and the  
211 Helsinki Lighthouse Tower (HLT) in the Gulf of Finland (Fig. 1). AERONET-OC measures the radiances of  
212 sun, sky and sea water at 412–1020 nm using the modified CIMEL Electronique CE-318 autonomous sun  
213 photometers, known as Sea-Viewing Wide Field-of-View Sensor (SeaWiFS) Photometer Revision for Incident

214 Surface Measurements (SeaPRISM). The system adopts a sea-viewing zenith angle of 140° and relative  
215 azimuth of 90° with respect to the sun in the successive observations at each waveband. Radiometric  
216 measurements in the first six wavebands (412–667 nm) are used to obtain water leaving radiance, while bands  
217 at 870 nm and 1020 nm are used for quality checks and turbid water flagging for the application of alternative  
218 above-water methods (Zibordi *et al.*, 2009b).

219 The AERONET-OC data are processed at three levels (Level 1.0, 1.5 and 2.0) based on different quality  
220 assurances, in which Level 2.0 is fully quality-controlled including pre- and post-field calibration with  
221 differences smaller than 5%, automatic cloud removal, and manual inspection. AERONET-OC Level 2.0 data  
222 at GDLT and HLT were obtained from <http://aeronet.gsfc.nasa.gov>. For the present validation, the normalized  
223 water-leaving radiances ( $L_{WN-f/Q}$ ) corrected for viewing angle dependence and for the effects of the  
224 non-isotropic distribution of the in-water radiance field, included in the AERONET-OC Level 2.0 data  
225 products, were selected (Fig. 2).

226 The AERONET-OC wavebands were designed for SeaWiFS which are slightly different to waveband  
227 centers for MERIS. The AERONET-OC waveband centers are 413, 441, 491, 555, 668 and 870 nm in HLT,  
228 and 412, 439, 500, 554, 675 and 870 nm in GDLT; while the related MERIS bands are centered at 412, 443,  
229 490, 560, 665 and 865 nm.  $L_{wn-f/Q}$  was band shift corrected based on regional bio-optical algorithms to reduce  
230 inter-band uncertainties. Further details of the methods are given in Zibordi *et al.* (2009a), where  $L_{WN-f/Q}$  is a  
231 function of the ratio of total backscattering and absorption coefficients, and of the extra-atmospheric solar  
232 irradiance. The calculation of  $R_{rs}$  is subsequently derived from  $L_{WN-f/Q}$  after band-shifting, as follows:

$$R_{rs}(\lambda) = \frac{L_{WN-f/Q}(\lambda)}{F_0(\lambda)} \quad (3)$$

233 where  $F_0$  is the extra-atmospheric solar irradiance for each waveband (Thuillier *et al.*, 2003).

234

#### 235 2.4 MERIS AC processors.

236 MERIS full resolution level 1b products (3rd reprocessing) segmented into 0.5° × 0.5° tiles around *in situ*  
237 measurements were processed using the following atmospheric correction schemes: CC (v1.8.3), C2R-Lakes  
238 (v1.6), C2R-CC (v 0.15), FUB (v 2.2), MEGS (v 8.1) and POLYMER (v 3.5). The first four atmospheric  
239 correction processors are based on artificial neural network algorithms to derive the atmospherically corrected  
240 water-leaving reflectance from TOA radiances. Ancillary data with actual sea surface pressure and total ozone

241 content values are utilized to calculate reflectance at the TOA. Water-leaving reflectance was estimated using  
242 the forward artificial neural network. The main differences between these four processors are the range of  
243 water constituents and inherent optical properties used in the datasets to train their respective neural networks.

244 The CC processor employed a wider range of optical properties in the training data (Doerffer and Schiller,  
245 2007), and was developed for application in optically-complex coastal waters. C2R (Doerffer & Schiller, 2007)  
246 was intended as a generic AC processor for complex Case 2 waters, and includes two plugins for the inland  
247 water constituent retrieval optimized for boreal and eutrophic lakes (Doerffer and Schiller, 2008). The training  
248 data set was produced through the ocean-atmosphere Monte Carlo photon tracing model. The atmospheric  
249 component of the model used a standard atmosphere (1013.2 hPa atmospheric pressure and 350 Dobson units  
250 of ozone) with different aerosol models, cirrus cloud particles and a rough, wind dependent sea surface with  
251 reflectance. The atmospheric correction for these two plugins is identical and hereafter we refer to them as  
252 C2R-Lakes. The atmospheric model for C2R-Lakes, in turn, was developed for optically complex inland and  
253 coastal waters using a calibration dataset specific to these environments. Similar to CC, a Monte Carlo  
254 radiative transfer model was used to simulate the TOA radiance, which contained four aerosols models  
255 (continental, maritime, urban / industrial and stratospheric). C2R-CC is the latest in the evolution of these  
256 processors, and employs artificial neural networks for atmospheric correction using a large training database  
257 obtained by radiative transfer simulations (Brockmann *et al.*, 2016). C2R-CC used a coastal aerosol model  
258 derived from coastal AERONET measurements (Aznay & Santer, 2009), and the atmospheric radiative  
259 transfer was calculated through a parameterised version of the successive order of scattering technique  
260 (Lenoble *et al.*, 2007). A version of C2R-CC specifically trained for extreme combinations of inherent optical  
261 properties is also included, but has not been considered here. FUB was designed for European coastal waters  
262 and integrates the entire AC process in a single neural network to retrieve water leaving reflectance from the  
263 TOA radiances. The data set used to train the neural network was generated by the matrix operator method,  
264 using a mixture of maritime and continental aerosol models as well as an US standard atmosphere (Schroeder  
265 *et al.*, 2007). The atmospheric correction scheme for FUB is divided into a Rayleigh-ozone correction and an  
266 atmospheric correction network. Water constituents and atmospheric properties are retrieved simultaneously  
267 from the TOA radiance, whereas the other processors firstly derive the reflectance, then calculate in-water  
268 parameters from the reflectance (Schroeder *et al.*, 2007). FUB provides the water-leaving reflectance at a  
269 subset of eight MERIS wavebands (412–665 nm and 709 nm).

270 MEGS was developed specifically for MERIS and has been regularly improved and updated, following

271 vicarious calibrations of MERIS. It performs the black-pixel atmospheric correction for open oceanic waters  
 272 with the low NIR  $R_{rs}$ , and uses the bright-pixel atmospheric correction for turbid waters based on the NIR  $R_{rs}$   
 273 with a fixed spectral shape (Antoine and Morel, 2011; Moore and Lavender, 2011). The optical properties of  
 274 atmospheric aerosol are inferred from the near-infrared wavebands and the atmospheric contribution to the  
 275 TOA signal is then extrapolated to the visible part of the spectrum. MEGS uses the spectra at near infrared  
 276 wavelengths (778 and 865 nm) to calculate the aerosol radiance ratio assuming that the reflectance is null at  
 277 the wavelength beyond 700 nm. The path radiance and its spectral shape in the visible wavebands is then  
 278 determined by iterating the different aerosol models and then validated using water-leaving reflectance at 510  
 279 nm assuming an a priori known constant for  $R_{rs}(510)$  (Nobileau and Antoine, 2005).

280 POLYMER is a spectral optimization method using a polynomial atmospheric model and a bio-optical  
 281 ocean water reflectance model. The atmospheric model simultaneously fits three components ranging from  
 282 spectrally neutral (e.g. residual sun glint) to weak ( $\lambda^{-1}$ , aerosols) and strong ( $\lambda^{-4}$ , e.g. Rayleigh scatter)  
 283 wavelength dependence. The bio-optical model only relies on Chl  $a$  concentration and the backscattering  
 284 coefficient of non-covarying particles (newer versions of POLYMER also include a mineral absorption  
 285 component, which is not considered relevant to the current data set). These five parameters are optimized to  
 286 obtain the best approximation of the measurements in a configurable range of spectral bands. Version 3.5 of  
 287 POLYMER was not specifically designed to handle optically complex coastal waters but includes a Case 2  
 288 water switch. The initial conditions for the Case-1 bio-optical model were changed to Chl  $a = 1 \text{ mg m}^{-3}$  and  
 289 total suspended matter =  $1 \text{ g m}^{-3}$  to avoid solutions designed for oceanic waters. The atmospheric model uses  
 290 the visible and NIR wavebands to assess sun glint and aerosol scattering properties (Steinmetz *et al.*, 2011). A  
 291 version of POLYMER (v4.1), with a modified bio-optical model which includes scattering by mineral particles  
 292 was trialed, but not considered to be a significant improvement for the low-mineral laden waters of the Baltic  
 293 Sea.

294 The main output of the six AC processors was the reflectance  $\rho_w(\lambda)$ , which was converted to  $R_{rs}(\lambda)$   
 295 following:

$$R_{rs}(\lambda) = \frac{\rho_w(\lambda)}{\pi} \quad (4)$$

296 A series of quality flags included with the output of each processor were used to define the validity of a  
 297 pixel either according to the input L1B data or as processor-specific conditions. Invalid pixels were masked  
 298 based on land, haze, whitecaps, cloud or sun glint contamination flags based on processing the L1B data with

299 Idepix v2.2.10. Processor specific flags included: poor fits to aerosol models; TOA radiances outside of the  
 300 training or application range; and results surpassing the minimum or maximum concentration bounds. The flag  
 301 combinations used with each processor are listed in Table 1.

302

303 Table 1. Quality flags for pixel exclusion criteria. l1 is level 1, l2 is level 2, l2r is level 2 reflectance, agc is atmospheric  
 304 sun glint correction, aot560 is aerosol optical thickness at 560 nm, oor is out of range, toa is top of atmosphere, tosa is top of  
 305 standard atmosphere, oos is out of scope, ooadb is aerosol model is out of aerosol model database, rtosa is reflectance at top of  
 306 standard atmosphere, atm\_in is atmospheric correction failure in input, atm\_out atmospheric correction failure in output,  
 307 pcd\_1\_13 is product confidence flag in bands 1 to 13, negative\_bb is negative backscatter.

processor	flags	Names
	l1_flags	suspect, land_ocean, bright, coastline, invalid
CC	l2r_flags	aot560_oor, toa_oor, tosa_oor, tosa_oos
C2R_Lake	agc_flags	atc_oor, toa_oor, tosa_oor
C2R-CC	l2_flags	rtosa_oor, rtosa_oos
FUB	result_flags	atm_in, atm_out
MEGS	l2_flags	ooadb, pcd_1_13
POLYMER	bitmask	negative_bb, out_of_bounds, exception

308

### 309 2.5 Match-up procedure

310 Match-ups between *in situ* and MERIS retrieved  $R_{rs}$  were selected based on location and overpass time, as  
 311 well as a spatial homogeneity criterion following Bailey and Werdell (2006), as outlined below.

312 Match-ups within  $\pm 12$  hours between *in situ* shipborne observations and MERIS over-pass were extracted  
 313 from the processed imagery in  $3 \times 3$  pixel boxes using the nearest neighbour approach. Subsequently match-up  
 314 time-windows of  $\pm 0.5$  h to  $\pm 12$  h were compared (Table 3) to obtain the best balance between the highest  
 315 number of match-ups and reducing artefacts such as water mass and particle dynamics (including  
 316 phytoplankton mobility). Due to the high sampling frequency from the ship, MERIS match-up pixels could  
 317 correspond to multiple shipborne observations. In these cases the mean ( $\mu$ ) and standard deviation ( $\sigma$ ) spectrum  
 318 of any valid *in situ* observations was calculated. *In situ* observations which exceeded  $\mu \pm 1.5\sigma$  were discarded  
 319 to decrease the effects of the horizontal (and to an extent, temporal) non-homogeneity. The mean spectrum of  
 320 the remaining observations matched to the same pixel was used for further analysis.

321 AERONET-OC Level 2.0 data were selected strictly within a  $\pm 2$ -h window around the satellite overpass.  
 322 The shorter time window was chosen because the AERONET-OC observations did not directly acquire  $E_d$  and  
 323 changing *in situ* illumination conditions could lead to invalid comparisons with  $R_{rs}$ . The AERONET-OC data  
 324 were obtained from the average in observations using the procedures outlined above to filter for outliers.

325 The  $3 \times 3$ -pixel boxes centered on the *in situ* locations were extracted from the atmospherically corrected  
 326 MERIS products. The MERIS retrieved  $R_{rs}$  were checked for spatial homogeneity to avoid the influence of  
 327 severe spatial variability and abnormal values. Differences between the value of each valid pixel and their  
 328 mean in the  $3 \times 3$ -pixel box were limited to twice the standard deviation to eliminate outliers. To meet the  
 329 spatial homogeneity criterion (filtered standard deviation divided by the filtered mean), the coefficient of  
 330 variation was set at  $< 0.15$ . If the number of remaining pixels in the  $3 \times 3$ -pixel box was less than 5, the  
 331 observation was omitted. The mean of remaining pixels in the  $3 \times 3$ -pixel box was then calculated.

332 Approximately 12% of the shipborne *in situ* observations remained after stringent quality control,  
 333 corresponding to 1947 individual MERIS pixels within the  $\pm 12$ -h window around the satellite overpass. The  
 334 number of shipborne observations available for match-up analysis decreased further after applying specific  
 335 quality flags for each AC processor. The number of match-up observations was 59 for CC, 602 for C2R-Lakes,  
 336 644 for C2R-CC, 256 for FUB, 427 for MEGS and 644 for POLYMER within the  $\pm 12$ -h window. From the  
 337 AERONET-OC Level 2 data approximately 22% of the available data (363 observations) corresponded to the  
 338  $\pm 2$ -h window around the satellite overpass, which were all used in subsequent analyses.

339 Figure 2 gives all shipborne and AERONET-OC data meeting these criteria. Measurements  $\pm 3$ -h for  
 340 shipborne data and  $\pm 2$ -h for AERONET-OC were subsequently used for accuracy assessment analysis given in  
 341 Figures 3-9 and to compute the statistics given in Table 4 and Figure 10a, c, d. The number of retrievals  
 342 differed for each AC processor. Table 5 and Figure 10b gives statistics using the same number of data for each  
 343 AC processor using a threshold of  $N = 494$ .

344

## 345 2.6 Statistical indices

346 The differences between MERIS observations and *in situ* observations were quantified using a number of  
 347 statistical metrics, including the coefficient of determination ( $R^2$ ), the average absolute percentage difference  
 348 ( $\psi$ ), the root-mean-square difference ( $\Delta$ ) and the bias ( $\delta$ ) between MERIS and *in situ* match-ups, calculated as  
 349 follows:

$$R^2 = \frac{(\sum (x_i - \bar{x})(y_i - \bar{y}))^2}{\sum (x_i - \bar{x})^2 \sum (y_i - \bar{y})^2} \quad (5)$$

$$\psi = \frac{1}{N} \sum_{i=1}^N \left| \frac{y_i - x_i}{x_i} \right| \times 100\% \quad (6)$$

$$\Delta = \sqrt{\frac{1}{N} \sum_{i=1}^N (y_i - x_i)^2} \quad (7)$$

$$\delta = \frac{1}{N} \sum_{i=1}^N \frac{y_i - x_i}{x_i} \quad (8)$$

350 where  $x_i$  is the  $i$ -th *in situ* observation,  $y_i$  is the  $i$ -th MERIS observation, and  $N$  is the number of match-ups.

351  $R^2$  is equal to the square of the correlation coefficient, representing a linear consistency between the *in*  
352 *situ* and MERIS observations, and the proportion of the variation that explained by the linear regression.  
353 Higher  $R^2$  indicates a higher degree of correlation, whereas  $R^2$  is sensitive to both outliers and narrow data  
354 distributions. Statistical significance of the correlation coefficient is tested using the student's distribution. The  
355 smaller the probability level of significance ( $p$ ), the more significant the linear relationship between *in situ* and  
356 MERIS observations.  $\Delta$  and  $\psi$  measures the accuracy of match-ups.  $\psi$  is the relative difference which is  
357 sensitive to small values while  $\Delta$  is the absolute difference which is sensitive to outliers. Values of  $\psi$  and  $\Delta$   
358 close to zero indicate that MERIS observations compare well with the *in situ* observations. Bias  $\delta$  is used to  
359 determine the underestimation or overestimation of MERIS products compared to the *in situ* data, with a value  
360 near zero indicating no systematic under- or over-estimation.

361 Type-2 linear regression was used to fit the *in situ* and MERIS observations for their independent  
362 randomness (Glover *et al.*, 2011; Brewin *et al.*, 2015). The slope ( $S$ ) close to one and intercept ( $I$ ) close to zero  
363 indicate that the MERIS observations fit well against the *in situ* observations.

364

### 365 2.7. AC processor ranking

366 A scoring scheme based on Brewin *et al.* (2015) and Müller *et al.* (2015) was employed to rank the  
367 relative performance of the AC processors. The score was obtained by comparing all statistical metrics ( $R^2$ ,  $\psi$ ,  
368  $\delta$ ,  $\Delta$ ,  $S$  and  $I$ ) for each waveband of each processor. The average score of all processors was compared against  
369 each individual processor. A score of  $<1$  or  $>1$  indicates significantly worse or better performance respectively.

370 A score ranging from zero to two for each statistical metric was assigned as follows:

371 (1) Zero points were assigned when: (i)  $R^2$  was less than the mean of the lower 90% confidence intervals  
372 of all processors; (ii) each of  $\psi$  and  $\Delta$  was higher than the mean of the upper 90% confidence interval; (iii)

373 each of  $\delta$  and  $I$  overlapped with neither the mean 90% confidence interval nor zero  $\pm$  twice the mean standard  
374 deviation; (iv)  $S$  overlapped with neither the mean 90% confidence interval nor one  $\pm$  twice the mean standard  
375 deviation.

376 (2) One point was assigned when: (i) each of  $R^2$ ,  $\psi$  and  $\Delta$  overlapped with the mean 90% confidence  
377 interval; (ii) each of  $\delta$  and  $I$  overlapped with either the mean 90% confidence interval or zero  $\pm$  twice the mean  
378 standard deviation, but not both; (iii)  $S$  overlapped with either the mean 90% confidence interval or one  $\pm$   
379 twice the mean standard deviation for all processors, but not both.

380 (3) Two points were assigned when: (i)  $R^2$  exceeded the upper limit of the mean 90% confidence interval;  
381 (ii) each of  $\psi$  and  $\Delta$  was less than the lower limit of the mean 90% confidence interval; (iii) each of  $\delta$  and  $I$   
382 overlapped with both the mean 90% confidence interval and zero  $\pm$  twice the mean standard deviation; (iv)  $S$   
383 overlapped with both the mean 90% confidence interval and one  $\pm$  twice the mean standard deviation.

384 For each waveband, a maximum of 12 points could be scored. Considering the varying numbers of  
385 wavebands returned by the six processors, the score was standardized to the sum of points by dividing over the  
386 number of wavebands. The final score for each processor was then obtained from the individual scores divided  
387 by the average score of all processors. The Monte Carlo method (Robert and Casella, 2013) was used over  
388 1000 repetitions, with the size of each re-sampled subset 0.75 times the size of the original dataset, to reduce  
389 the sensitivity of the scores to the size of the matched dataset available with each processor. Monte Carlo  
390 resampling resulted in a confidence range of the score for each AC processor.

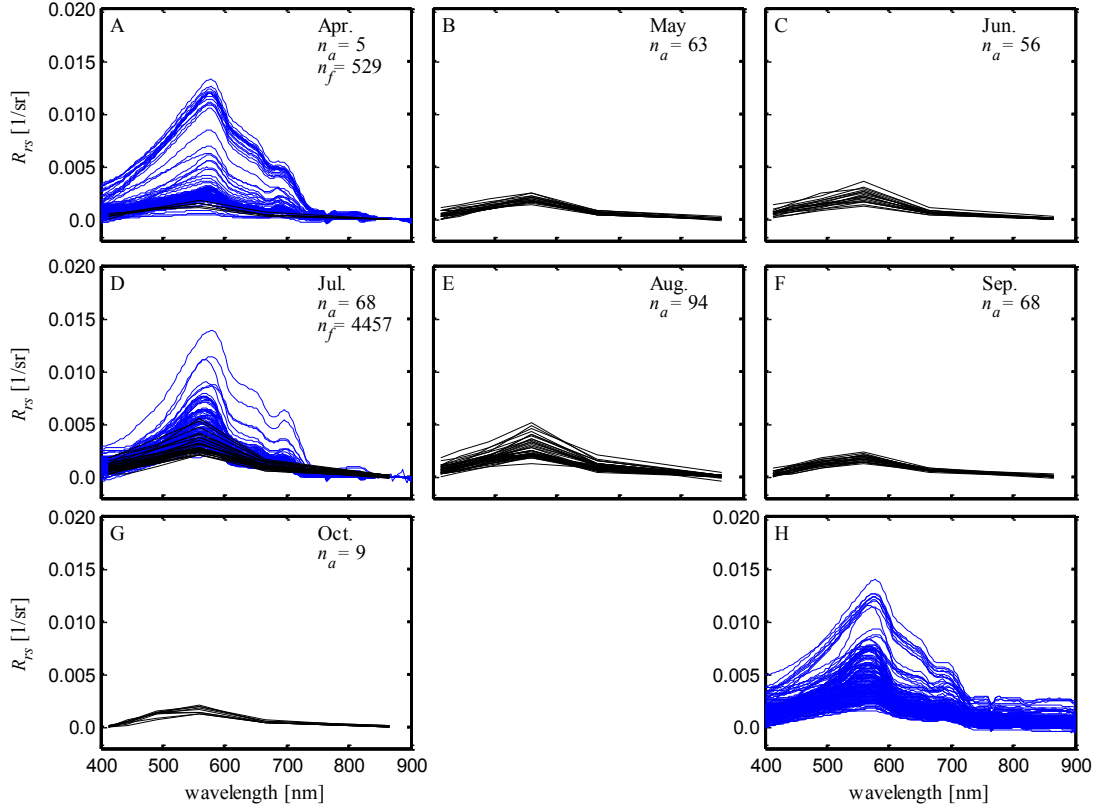
391

### 392 **3. Results**

#### 393 *3.1. Offset correction for the shipborne observations*

394 Fig. 2 presents the *in situ*  $R_{rs}$  spectra observed from the AERONET-OC and shipborne platforms. The two  
395 data sources may differ slightly since the AERONET-OC observations are taken from a stationary tower where  
396 the sensors are located some  $\sim$ 25 m from the sea surface with a field of view of  $1^\circ$ . The shipborne observations  
397 were located  $\sim$ 7 m from the sea surface with the field of view of  $7^\circ$ . The spectra measured from the shipborne  
398 platform are given in Fig. 2H and  $R_{rs}(865)$  was  $> 0.0020 \text{ sr}^{-1}$  for many spectra. These values are significantly  
399 higher than those reported in Ficek *et al.* (2011) and in most cases greater than the ranges obtained from the  
400 MERIS atmospheric correction processors for  $R_{rs}(865)$  (Figs. 3–8). Spectra in panels A-G have been  
401 offset-corrected by subtracting the average  $R_{rs}$  at 850–900 nm from each reflectance spectrum.

402



403  
 404 Fig. 2. Spectra of remote-sensing reflectance  $R_{rs}(\lambda)$  observed from the ship (blue curves) and AERONET-OC (black curves),  
 405 separated by month in panels A-G. Panel H shows the shipborne  $R_{rs}$  spectra before applying a near infra-red offset correction.  
 406 The number of observations are marked  $n_a$  and  $n_f$  for the AERONET-OC and shipborne  $R_{rs}$  (following quality control),  
 407 respectively.

408  
 409 Basic match-up statistics between MERIS-derived  $R_{rs}(\lambda)$  and both offset-corrected and uncorrected  
 410 shipborne observations are given in Table 2. For the match-ups between MERIS and shipborne observations,  $\Delta$   
 411 of the non-offset corrected  $R_{rs}$  at selected MERIS wave bands varied from 0.0009  $\text{sr}^{-1}$  to 0.0078  $\text{sr}^{-1}$  for CC,  
 412 while the range was 0.0004–0.0011  $\text{sr}^{-1}$  for other processors. Using the offset corrected data, the difference was  
 413 greater for CC ( $\Delta = 0.0011$ –0.0080  $\text{sr}^{-1}$ ), but lower for all other processors ( $\Delta = 0.0002$ –0.0011  $\text{sr}^{-1}$ ). The  
 414 determination coefficients  $R^2$  increased and the correlation was improved for each processor following the  
 415 offset correction. From hereon, the *in situ* shipborne  $R_{rs}$  are reported exclusively using the offset correction.  
 416 We note that the use of a spectrally neutral offset correction is suitable in combination with the fingerprint  
 417 method used to calculate shipborne  $R_{rs}(\lambda)$ , which is discussed further in section 4.1.

418  
 419 Table 2  
 420 The root mean square difference ( $\Delta$ , units  $\text{sr}^{-1}$ ) and the coefficient of determination ( $R^2$ ) between  $R_{rs}$  derived from MERIS and *in*  
 421 *situ* shipborne observations using a match-up time window of  $\pm 3\text{h}$ , using no offset and offset correction.

---

$\Delta$  ( $R^2$ )

---

No offset correction	443 nm	490 nm	560 nm	665 nm	709 nm
CC	0.0054 (0.00)	0.0068 (0.55)	0.0078 (0.63)	0.0018 (0.01)	0.0009 (0.01)
C2R-Lakes	0.0005 (0.40)	0.0006 (0.62)	0.0006 (0.88)	0.0004 (0.58)	0.0004 (0.40)
C2R-CC	0.0007 (0.20)	0.0007 (0.57)	0.0009 (0.79)	0.0004 (0.56)	0.0004 (0.44)
FUB	0.0006 (0.40)	0.0006 (0.79)	0.0011 (0.86)	0.0008 (0.35)	0.0006 (0.01)
MEGS	0.0011 (0.25)	0.0009 (0.61)	0.0008 (0.83)	0.0006 (0.44)	0.0005 (0.36)
POLYMER	0.0007 (0.44)	0.0005 (0.79)	0.0007 (0.88)	0.0004 (0.50)	0.0006 (0.31)
Offset correction	443 nm	490 nm	560 nm	665 nm	709 nm
CC	0.0056 (0.30)	0.0070 (0.47)	0.0080 (0.53)	0.0021 (0.64)	0.0011 (0.73)
C2R-Lakes	0.0005 (0.40)	0.0007 (0.65)	0.0005 (0.91)	0.0003 (0.78)	0.0002 (0.66)
C2R-CC	0.0008 (0.23)	0.0008 (0.62)	0.0008 (0.80)	0.0003 (0.71)	0.0003 (0.63)
FUB	0.0004 (0.51)	0.0003 (0.87)	0.0008 (0.88)	0.0004 (0.76)	0.0003 (0.61)
MEGS	0.0011 (0.22)	0.0009 (0.62)	0.0008 (0.85)	0.0004 (0.62)	0.0004 (0.62)
POLYMER	0.0009 (0.54)	0.0006 (0.88)	0.0006 (0.91)	0.0003 (0.80)	0.0003 (0.67)

422

### 423 3.2. *In situ* $R_{rs}$

424 The monthly AERONET-OC spectral reflectance over the visible and near-infrared domains exhibited a  
425 high degree of similarity (Fig. 2 A–G). The hyperspectral  $R_{rs}$  collected from the shipborne measurements  
426 covered a wider  $R_{rs}$  range, but were largely restricted to observations in April and July when the research  
427 cruises primarily targeted the period of highest chlorophyll *a*.

428 A dominant peak in the reflectance between 500 to 600 nm is seen in all AERONET-OC spectra. The  
429 amplitude of reflectance was consistently low with the maxima  $< 0.006 \text{ sr}^{-1}$  around 550 nm and the minima  
430 approaching zero in the blue waveband at 412 nm, indicating high absorption by CDOM. Monthly average  
431  $R_{rs}(550)$  changed seasonally with the lower values of  $0.0017 \text{ sr}^{-1}$  in May and September, and with the higher  
432 values of  $0.0029 \text{ sr}^{-1}$  in July and August.

433

434 Table 3

435 Statistical results of  $R_{rs}(560)$  between MERIS and shipborne observations for six match-up time windows of  $\pm 0.5 \text{ h}$ ,  $\pm 2 \text{ h}$ ,  $\pm 3 \text{ h}$ ,  
436  $\pm 4 \text{ h}$ ,  $\pm 6 \text{ h}$  and  $\pm 12 \text{ h}$ , including the number of match-ups ( $N$ ), the determination coefficient ( $R^2$ ), the average absolute  
437 percentage difference ( $\psi$ ), the root mean square difference ( $\Delta$ ) and the bias ( $\delta$ ).

		Time window					
		$\pm 0.5 \text{ h}$	$\pm 2 \text{ h}$	$\pm 3 \text{ h}$	$\pm 4 \text{ h}$	$\pm 6 \text{ h}$	$\pm 12 \text{ h}$
CC	$N$	4	26	40	40	52	59
	$R^2$	1.00	0.56	0.53	0.53	0.13	0.08
	$\psi$ (%)	240.95	215.56	246.10	246.10	219.57	211.65
	$\Delta$	0.0077	0.0073	0.0080	0.0080	0.0076	0.0074

	$\delta$	2.41	2.13	2.45	2.45	2.14	2.07
C2R-lakes	$N$	81	245	420	490	544	602
	$R^2$	0.91	0.92	0.91	0.87	0.86	0.85
	$\psi$ (%)	8.85	9.77	9.03	9.70	10.46	10.44
	$\Delta$	0.0004	0.0005	0.0005	0.0006	0.0006	0.0006
	$\delta$	0.05	0.07	0.05	0.05	0.05	0.04
C2R-CC	$N$	86	265	453	534	578	644
	$R^2$	0.91	0.87	0.80	0.75	0.70	0.69
	$\psi$ (%)	9.79	14.07	14.51	16.49	16.56	17.39
	$\Delta$	0.0004	0.0007	0.0008	0.0008	0.0009	0.0009
	$\delta$	-0.03	-0.07	-0.03	-0.04	-0.02	-0.03
FUB	$N$	43	149	221	255	255	256
	$R^2$	0.61	0.85	0.88	0.87	0.87	0.86
	$\psi$ (%)	22.36	21.36	18.20	18.40	18.41	18.56
	$\Delta$	0.0009	0.0008	0.0008	0.0009	0.0009	0.0009
	$\delta$	-0.22	-0.17	-0.14	-0.15	-0.15	-0.15
MEGS	$N$	74	201	306	364	377	427
	$R^2$	0.92	0.88	0.85	0.77	0.76	0.76
	$\psi$ (%)	7.11	12.28	12.05	12.89	13.09	14.79
	$\Delta$	0.0004	0.0007	0.0008	0.0009	0.0009	0.0009
	$\delta$	0.02	-0.03	-0.01	-0.02	-0.02	-0.05
POLYMER	$N$	95	281	453	518	573	644
	$R^2$	0.98	0.93	0.91	0.87	0.85	0.83
	$\psi$ (%)	5.47	9.19	8.63	9.10	9.48	11.51
	$\Delta$	0.0002	0.0005	0.0006	0.0006	0.0007	0.0008
	$\delta$	-0.03	-0.05	-0.03	-0.03	-0.03	-0.06

438

439 The shipborne hyperspectral  $R_{rs}$  observation showed a similar spectral shape, with the green peak located  
440 near 580 nm, with a maximum  $< 0.015 \text{ sr}^{-1}$ . A local minimum at 660 nm and maximum at 680 nm were  
441 consistently observed in the shipborne hyperspectral  $R_{rs}$ , corresponding to the absorption of Chl *a* in the red  
442 waveband (675 nm) and sun-induced fluorescence of Chl *a*, respectively. Spectra in July and August also had  
443 the highest absorption at red wavebands when Chl *a* concentrations reached up to  $15 \text{ mg m}^{-3}$  (Simis & Olsson,  
444 2013).

445

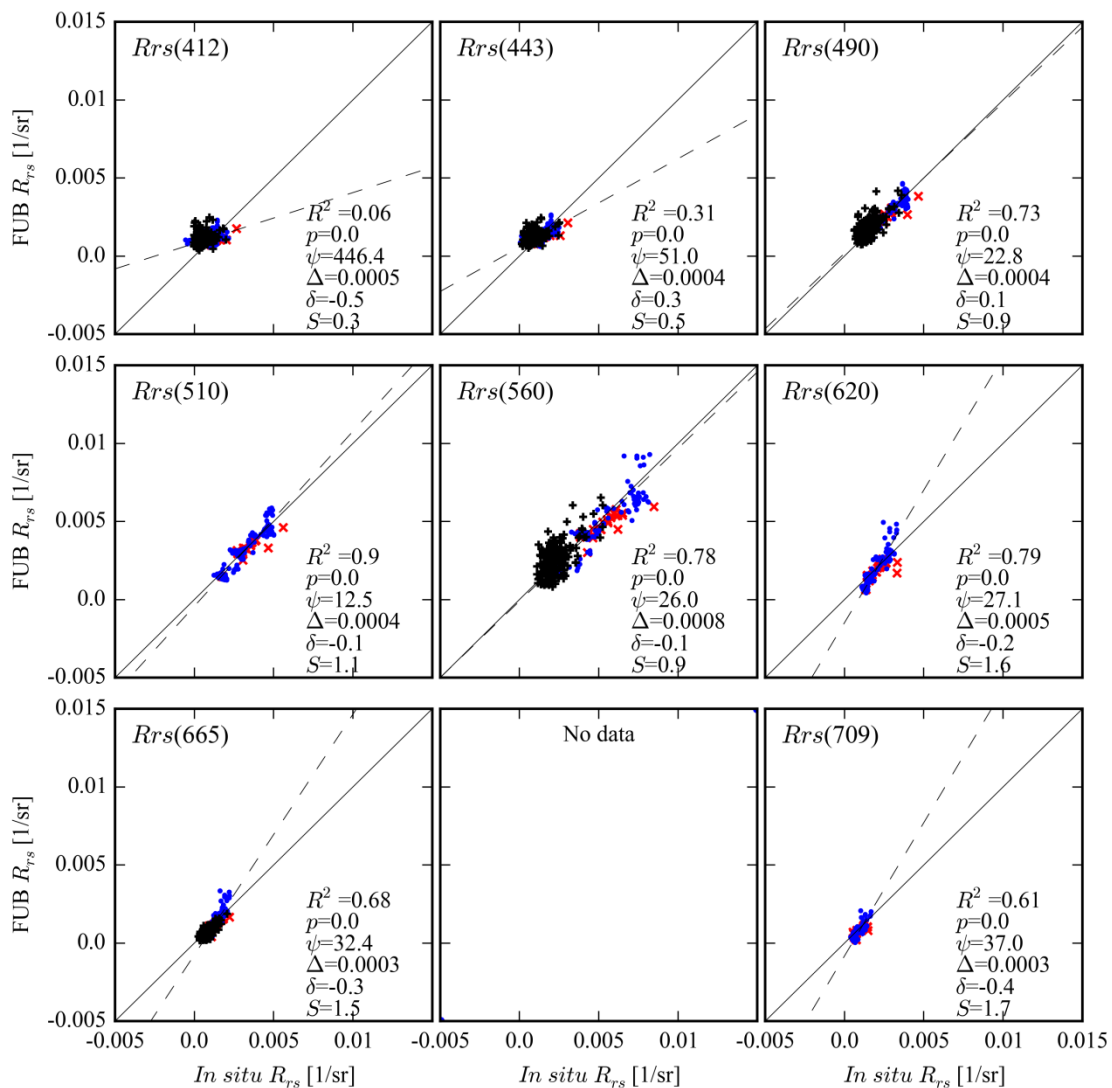
### 446 3.3. Match-up time window of the shipborne observations

447 We analyzed various time windows ( $\pm 12 \text{ h}$ ,  $\pm 6 \text{ h}$ ,  $\pm 4 \text{ h}$ ,  $\pm 3 \text{ h}$ ,  $\pm 2 \text{ h}$  and  $\pm 0.5 \text{ h}$ ) between the shipborne data  
448 and MERIS over-pass to assess the effect on the match-up results, which are given in Table 3 for  $R_{rs}(560)$ .

449 Compared to the  $\pm 12\text{-h}$  window, the number of match-ups decreased to 90% for the  $\pm 6\text{-h}$  window, 83 %

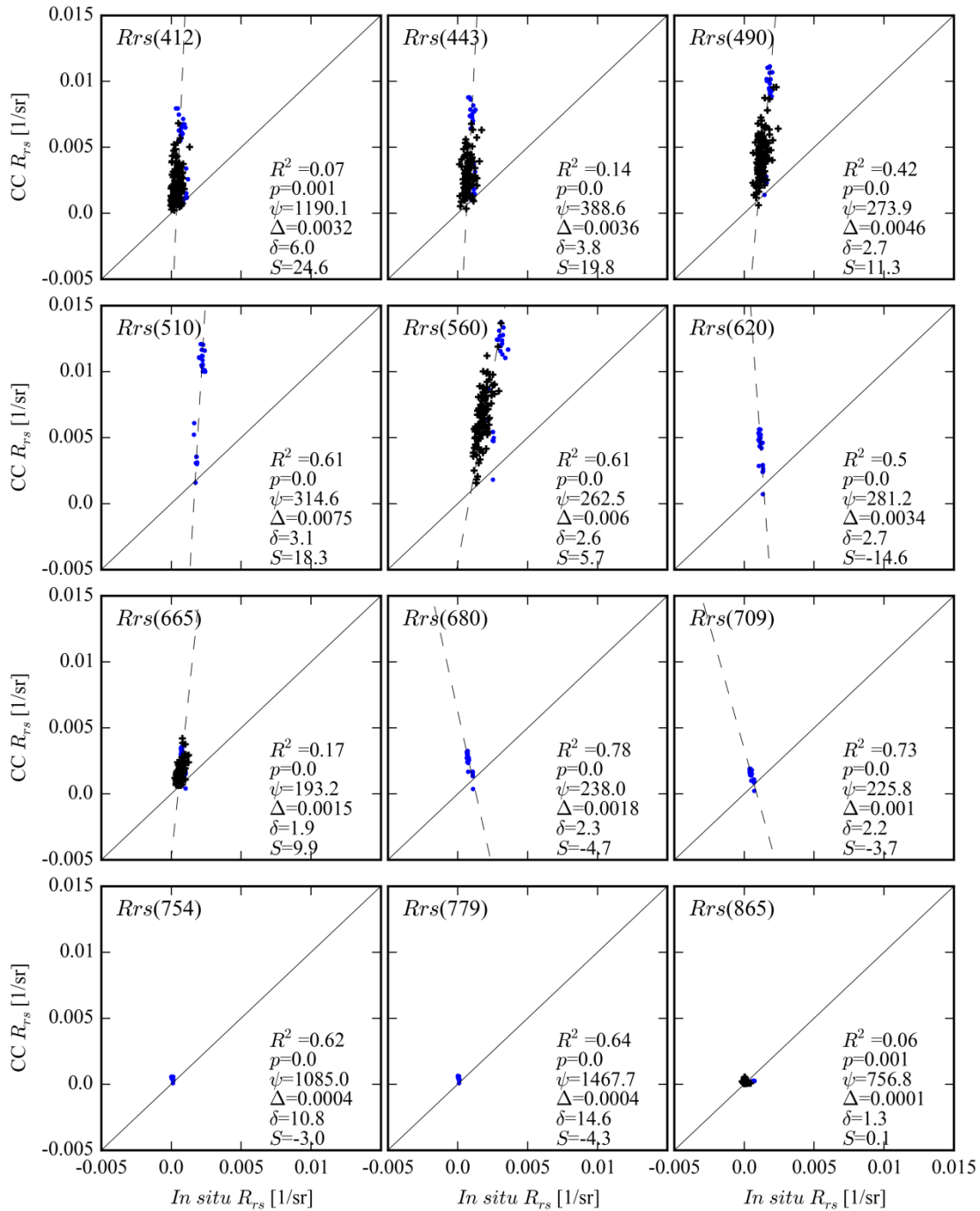
450 for the  $\pm 4$ -h window, 73% for the  $\pm 3$ -h window, 46% for the  $\pm 2$ -h window and 14% for the  $\pm 0.5$ -h window.  
 451 The  $\psi$  values of  $R_{rs}(560)$  by POLYMER ranged from 5.5% ( $\pm 0.5$ -h window) up to 11.5% ( $\pm 12$ -h window) and  
 452  $\Delta$  were from  $0.0002 \text{ sr}^{-1}$  to  $0.0008 \text{ sr}^{-1}$ . Analogous results were observed for C2R-Lakes, C2R-CC and MEGS.  
 453 The number of match-ups was lower for these processors and MERIS  $R_{rs}(560)$  showed a lower difference with  
 454 the *in situ*  $R_{rs}$  when using the shorter time windows. For the shorter match-up windows, the coefficient of  
 455 determination improved for most processors except for CC and FUB, while the bias varied slightly for all  
 456 processors.  $R_{rs}(560)$ , irrespective of AC processor, had the lowest deviation when using the  $\pm 3$ -h match-up  
 457 window. Similar performance was observed for the other wavebands. The time window of  $\pm 3$  h was selected to  
 458 report further results, providing the best balance between match-up volume and statistical match-up  
 459 performance.

460



461

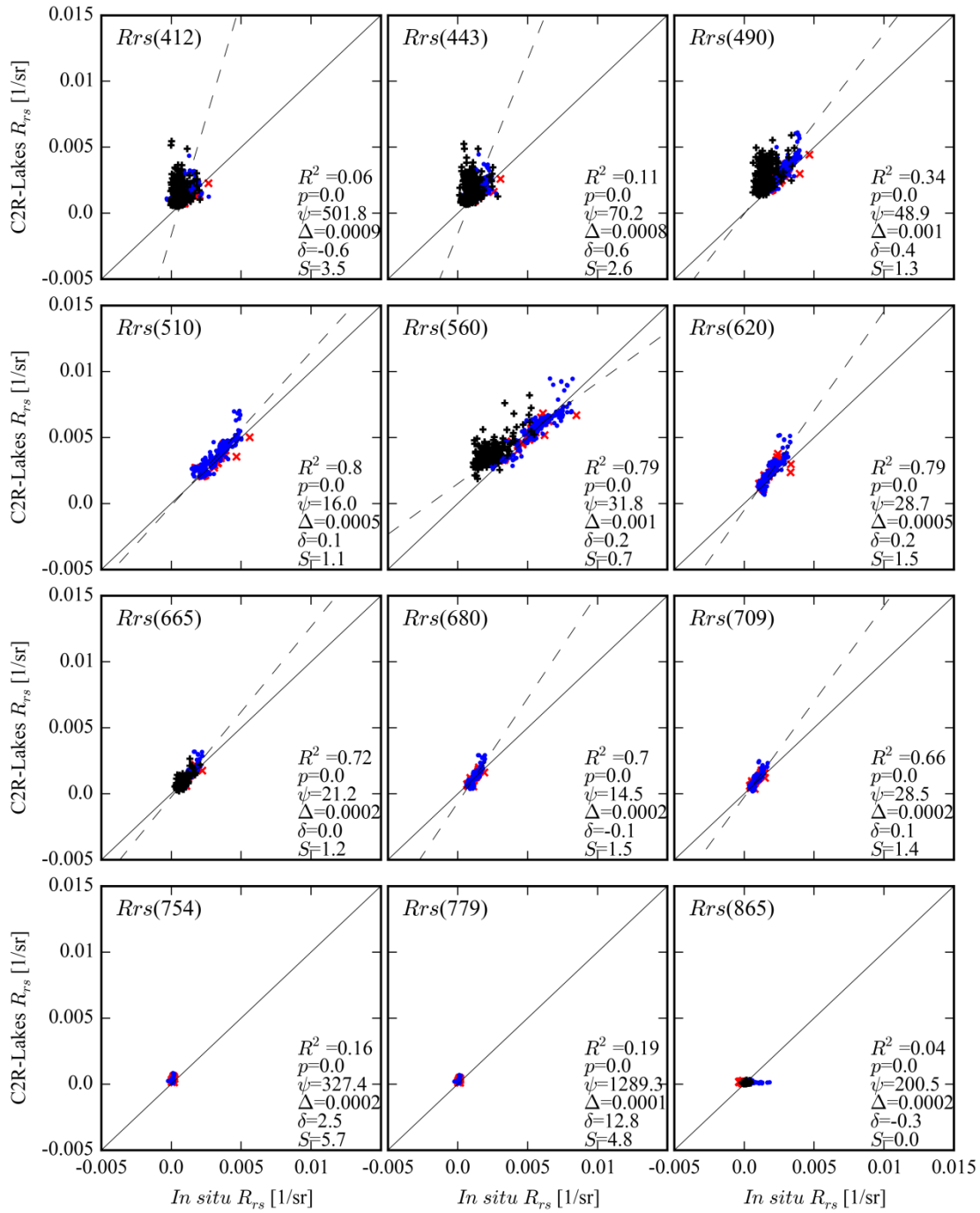
462 Fig. 3. Scatter plots of MERIS  $R_{rs}$  retrieved by FUB versus *in situ*  $R_{rs}$ , for MERIS bands as indicated at the top of each panel. The  
 463 number of observations are  $n_a = 176$  for the AERONET-OC and  $n_f = 221$  for shipborne  $R_{rs}$ . Blue points represent match-ups with  
 464 shipborne data, red crosses are shipborne observations where  $R_{rs}$  was negative in the near infra-red (before offset correction), and  
 465 black plusses are match-ups with AERONET-OC. The solid line represents unity and the dashed line is the best fit of Type-2  
 466 linear least-squares regression through the combined data sets.  $R^2$  is the coefficient of determination,  $p$  is the probability level of  
 467 significance,  $\psi$  is the average absolute percentage difference,  $\Delta$  is the root mean square difference and  $\delta$  is the bias between  
 468 MERIS and *in situ* match-ups,  $S$  is the slope of the Type-2 linear regression.  
 469  
 470



471  
 472 Fig. 4. Scatter plots of  $R_{rs}$  retrieved by CC versus *in situ*  $R_{rs}$ . The number of observations are  $n_a = 110$  for the AERONET-OC and  $n_f$

473 = 40 for shipborne  $R_{rs}$ . Markers and symbols are as described for Fig. 3.

474



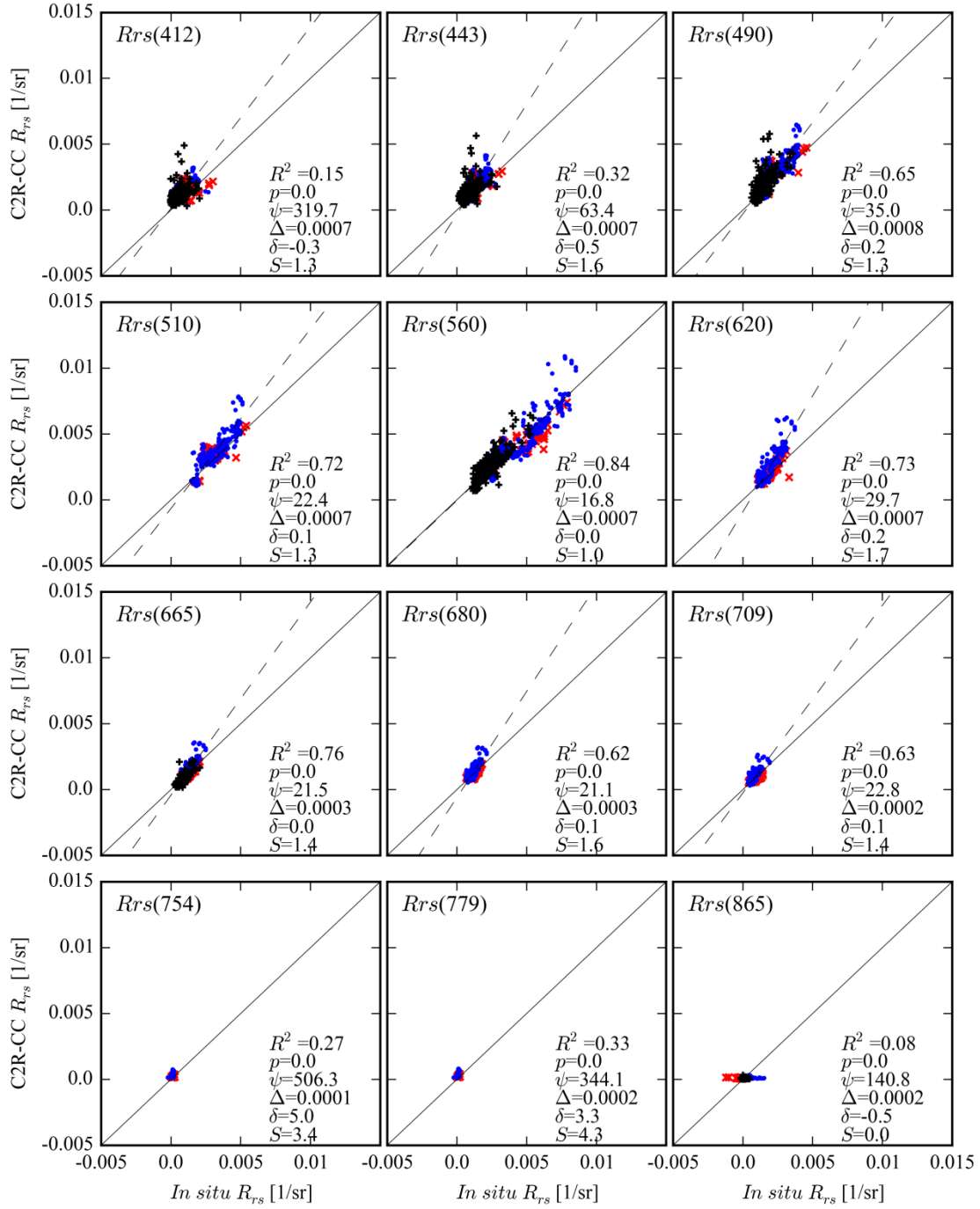
475

476 Fig. 5. Scatter plots of  $R_{rs}$  retrieved by C2R-Lakes versus *in situ*  $R_{rs}$ . The number of observations are  $n_a = 213$  for the

477 AERONET-OC and  $n_f = 420$  for shipborne  $R_{rs}$ . Markers and symbols are as described for Fig. 3.

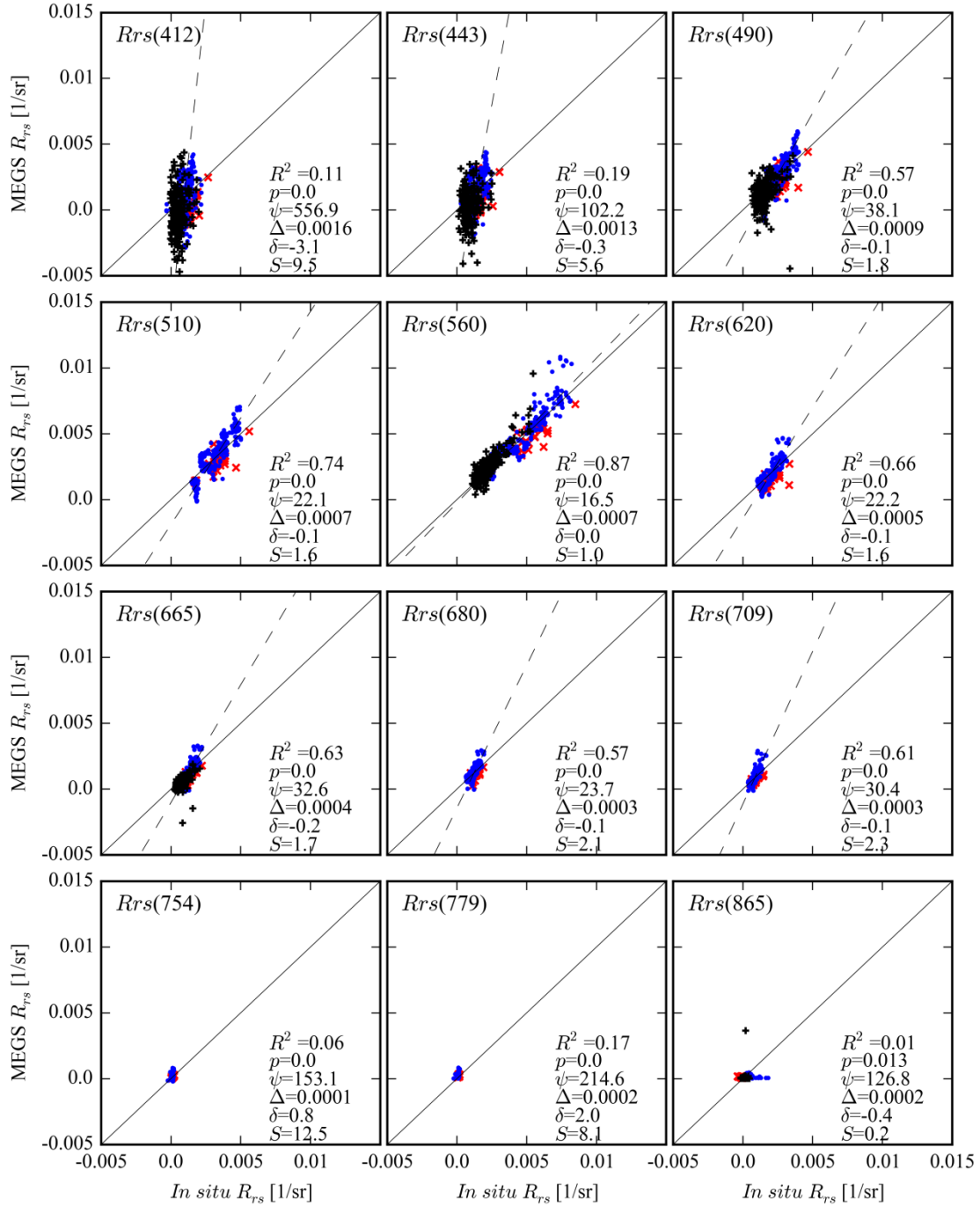
478

479

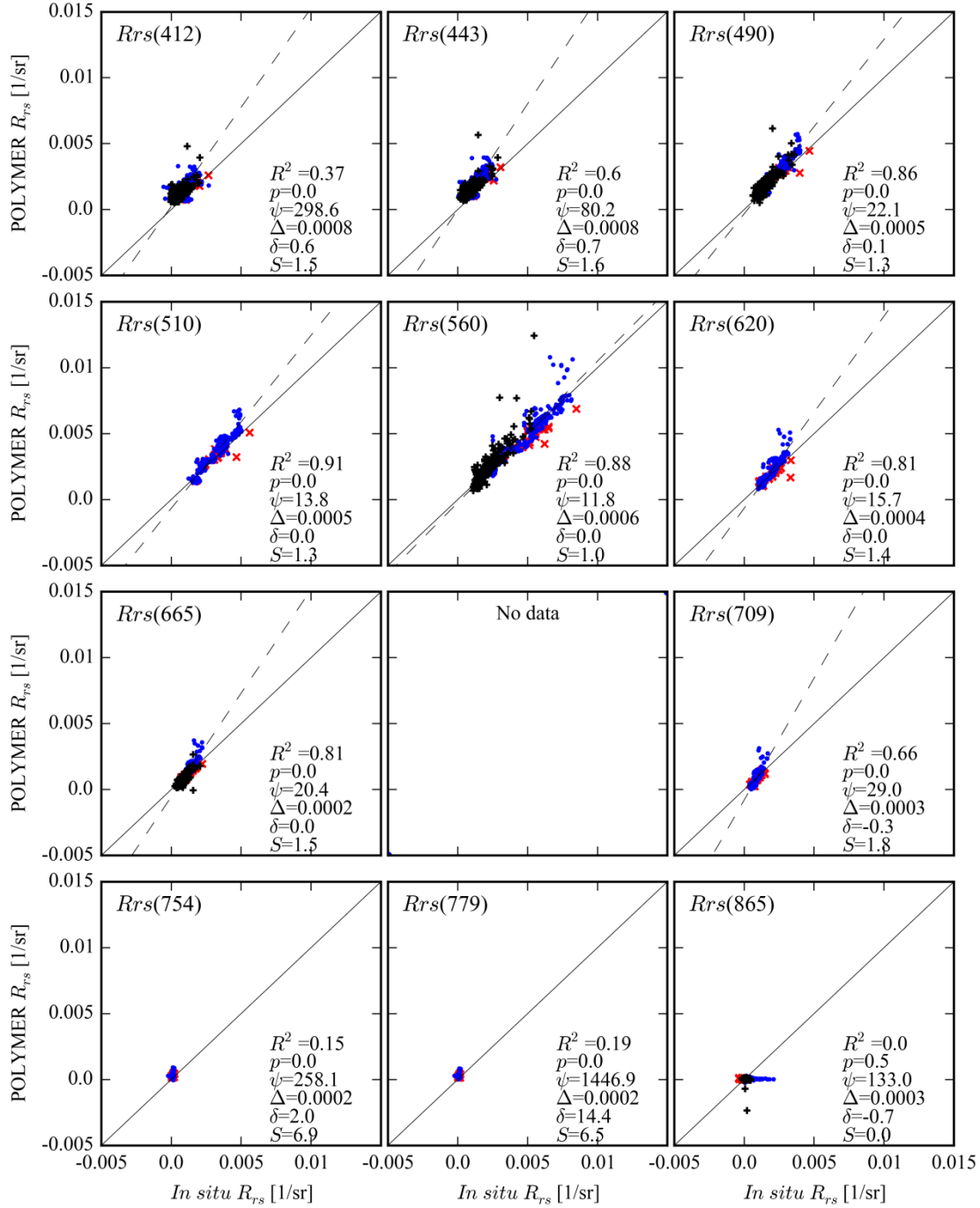


480  
 481 Fig. 6. Scatter plots of  $R_{rs}$  retrieved by C2R-CC versus *in situ*  $R_{rs}$ . The number of observations are  $n_a = 214$  for the AERONET-OC  
 482 and  $n_f = 453$  for shipborne  $R_{rs}$ . Markers and symbols are as described for Fig. 3.

483  
 484



485  
 486 Fig. 7. Scatter plots of  $R_{rs}$  retrieved by MEGS versus *in situ*  $R_{rs}$ . The number of observations are  $n_a = 187$  for the AERONET-OC  
 487 and  $n_f = 306$  for shipborne  $R_{rs}$ . Markers and symbols are as described for Fig. 3.



488

489 Fig. 8. Scatter plots of  $R_{rs}$  retrieved by POLYMER versus *in situ*  $R_{rs}$ . The number of observations are  $n_a = 211$  for the  
 490 AERONET-OC and  $n_f = 453$  for shipborne  $R_{rs}$ . Markers and symbols are as described for Fig. 3.

491

### 492 3.4. Accuracy assessment of AC processors

493 Firstly, all valid match-up observations within  $\pm 3$ -h for shipborne data and  $\pm 2$ -h for AERONET-OC were  
 494 considered for each of the processors. All six AC processors showed a low correlation at 412 nm ( $R^2 < 0.37$ ),  
 495 significant probability of the regression fit ( $p < 0.001$ ) and large deviations ( $\psi > 200\%$ ) with *in situ*  $R_{rs}$

496 match-ups (Figs. 3–8). It is noted that the range in *in situ*  $R_{rs}$  at blue bands was small, which influences these  
 497 regression results. For C2R-Lakes, C2R-CC, FUB, MEGS and POLYMER  $R_{rs}(443)$ , there was a slightly  
 498 higher correlation ( $R^2$  ranging from 0.11 to 0.60) and lower differences ( $\psi$  ranging from 51% to 102%)  
 499 compared to *in situ*  $R_{rs}(443)$ , except for CC. The highest relative differences of all processors were observed in  
 500 the near infrared at 754 and 779 nm with  $\psi > 150\%$ . For the other visible wavebands (490–709 nm), the  
 501 performance of all processors improved, especially FUB, C2R-Lakes, C2R-CC, MEGS and POLYMER (Figs.  
 502 3, 5, 6, 7 and 8). The FUB processor performed well at 490–709 nm with  $R^2 > 0.61$  and low  $\psi$  of 12–37% (Fig.  
 503 3). Compared to all *in situ*  $R_{rs}(\lambda)$ , the CC processor over-estimated  $R_{rs}$  with a high positive bias ( $\delta > 1.9$ ),  
 504 which resulted in the highest differences ( $\psi > 190\%$ ) in visible wavebands (Fig. 4). The C2R-Lakes processor  
 505 showed good agreement with *in situ*  $R_{rs}(\lambda)$  for most bands with  $\psi < 30\%$  and  $R^2 = 0.66–0.80$ , but exhibited  
 506 high differences at 490 nm ( $\psi = 49\%$ ) and 560 nm ( $\psi = 32\%$ ). C2R-CC also performed well and had low  $\psi$   
 507  $< 35\%$  in bands 490–709 nm and a moderate coefficient of determination ( $R^2$  ranging from 0.62 to 0.84).  
 508 MEGS had a low correlation at most wavebands ( $R^2 < 0.74$ ) and similar deviations with  $\psi = 22–38\%$ , except  
 509 for  $R_{rs}(560)$  with a better performance ( $\psi = 16\%$  and  $R^2 = 0.87$ ). POLYMER was the most accurate processor  
 510 with lowest  $\psi$  (12% to 22%) and highest consistency ( $R^2 > 0.81$ ), except for  $R_{rs}(709)$  with lower accuracy ( $\psi =$   
 511 29%,  $R^2 = 0.66$ ).

512

513 Table 4

514 The numbers of observations shared between any two AC processors.

	CC	FUB	C2R-lakes	C2R-CC	MEGS	POLYMER
CC	150					
FUB	101	397				
C2R-lakes	150	355	633			
C2R-CC	150	396	622	667		
MEGS	118	336	495	494	495	
POLYMER	150	397	632	664	495	664

515

516 There was a large variation in the number of valid match-ups between processors with 150 for CC, 633  
 517 for C2R-Lakes, 667 for C2R-CC, 397 for FUB, 495 for MEGS and 664 for POLYMER. We therefore also  
 518 compared performance over the set of match-ups shared by the processors to reduce the effect of  
 519 processor-specific quality flags. Table 4 gives an overview of the number of observations shared between any  
 520 two AC processors within the  $\pm 3$ -h window. CC and FUB had the lowest number of valid observations, which  
 521 indicates that these two processors were often operating out of their scope and may not be applicable to the

522 Baltic Sea. When CC and FUB are not considered, the shared subset of match-ups for C2R-Lakes, C2R-CC,  
 523 MEGS and POLYMER was 494 and the statistical results at  $R_{rs}$  490, 560, 620, 665 and 709 nm is given in  
 524 Table 5.

525

526 Table 5

527 Statistical results of  $R_{rs}$  match-ups based on 494 shared observations within a time window of  $\pm 3$  h, including the coefficient of  
 528 determination ( $R^2$ ), the average absolute percentage difference ( $\psi$ ), the root mean square difference ( $\Delta$ ), and bias ( $\delta$ ), slope ( $S$ )  
 529 and intercept ( $I$ ) of type-2 linear regression between MERIS and *in situ* match-ups.

processor	$\lambda$ (nm)	$R^2$	$\psi$ (%)	$\Delta$ (sr <sup>-1</sup> )	$\delta$	$S$	$I$ (sr <sup>-1</sup> )
C2R-Lakes	490	0.35	53.75	0.0012	0.52	1.21	0.0004
	510	0.78	17.52	0.0006	0.15	1.09	0.0001
	560	0.81	35.25	0.0011	0.33	0.75	0.0017
	620	0.78	28.33	0.0006	0.20	1.64	-0.0008
	665	0.71	22.99	0.0003	0.08	1.31	-0.0003
	680	0.66	16.34	0.0003	-0.02	1.95	-0.0012
	709	0.62	27.67	0.0003	0.12	1.71	-0.0005
C2R-CC	490	0.73	31.08	0.0008	0.23	1.39	-0.0004
	510	0.82	17.78	0.0007	0.09	1.47	-0.0012
	560	0.85	17.06	0.0008	0.00	1.03	-0.0002
	620	0.73	27.76	0.0008	0.23	2.08	-0.0016
	665	0.78	20.89	0.0003	0.03	1.56	-0.0006
	680	0.64	20.42	0.0004	0.07	2.11	-0.0013
	709	0.62	21.39	0.0003	0.10	1.81	-0.0006
MEGS	490	0.57	38.19	0.0009	-0.08	1.87	-0.0020
	510	0.74	22.15	0.0008	0.00	1.62	-0.0019
	560	0.87	16.54	0.0007	0.05	1.10	-0.0003
	620	0.66	22.33	0.0005	-0.08	1.69	-0.0014
	665	0.63	32.66	0.0004	-0.19	1.79	-0.0010
	680	0.57	23.80	0.0004	-0.01	2.18	-0.0015
	709	0.62	30.39	0.0004	-0.03	2.33	-0.0011
POLYMER	490	0.87	22.05	0.0006	0.17	1.31	-0.0003
	510	0.90	13.44	0.0005	0.07	1.34	-0.0008
	560	0.87	12.89	0.0007	0.02	1.08	-0.0002
	620	0.79	15.19	0.0005	0.06	1.58	-0.0010
	665	0.83	21.07	0.0003	0.00	1.60	-0.0006
	709	0.65	26.95	0.0003	-0.15	2.10	-0.0010

530

531 For this data set, C2R-Lakes tended to overestimate  $R_{rs}$  from 510–709 nm where  $\delta$  varied from -0.02 to  
 532 0.33 and  $\psi$  was  $< 35\%$ .  $R_{rs}(490)$  showed higher deviation with  $\psi = 54\%$  and  $R^2 = 0.35$  (Table 5). C2R-CC  
 533 tended to overestimate  $R_{rs}$  with  $\delta$  between 0.00 and 0.23 at 490 to 709 nm, with  $\psi < 31\%$ . MEGS

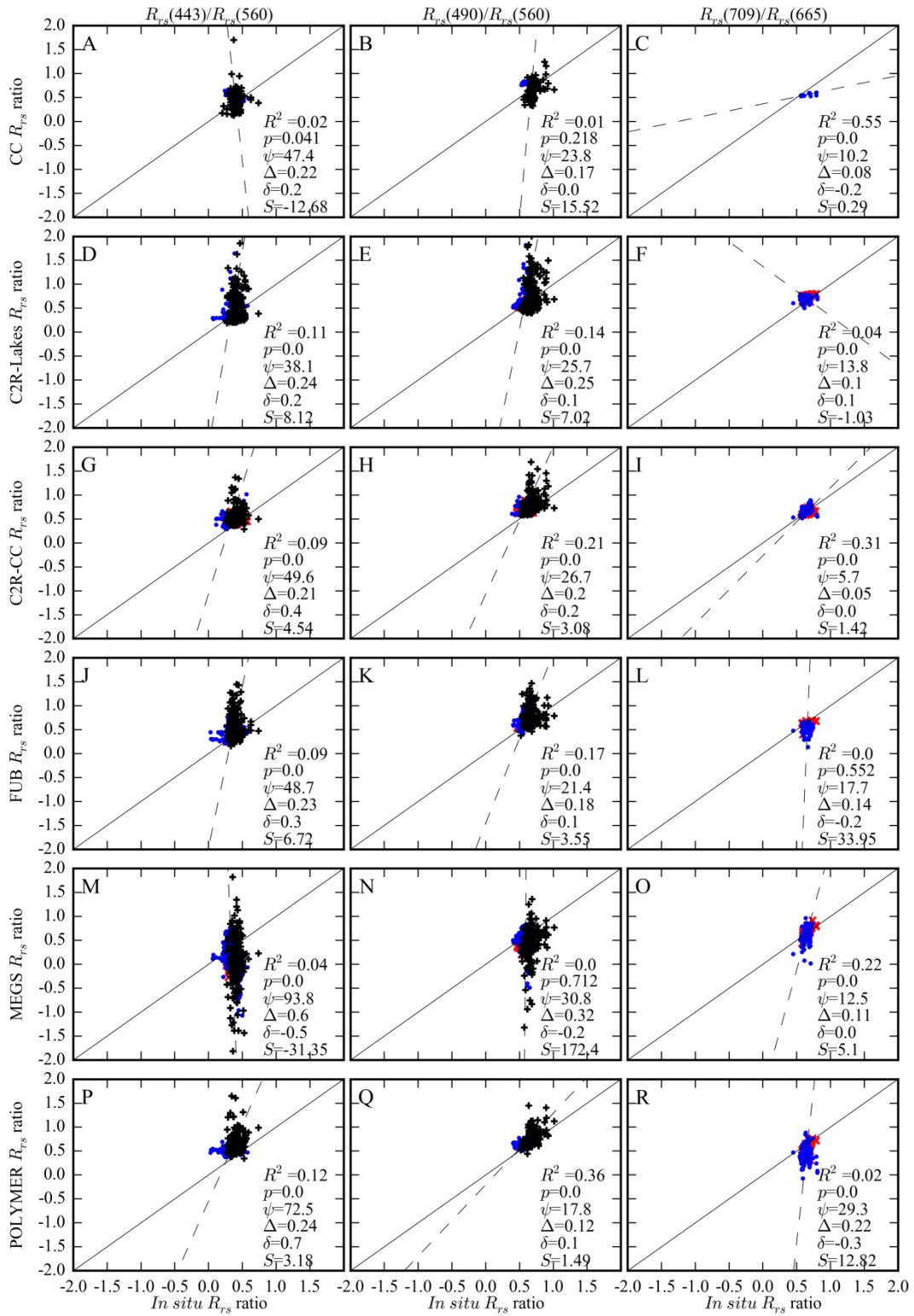
534 underestimated  $R_{rs}$  especially at 620 to 709 nm, with a moderate correlation ( $R^2 = 0.57\text{--}0.74$ ) and  $\psi$  varying  
535 from 22% to 38%, except for  $R_{rs}(560)$  where  $R^2 = 0.87$  and  $\psi = 17\%$ . The highest correlation with *in situ*  $R_{rs}$   
536 was for POLYMER which gave  $R^2 > 0.65$  and  $\psi < 27\%$  at these wavebands.

537

### 538 3.5. Accuracy assessment of band ratios

539 Band ratios  $R_{rs}(443)/R_{rs}(560)$ ,  $R_{rs}(490)/R_{rs}(560)$  and  $R_{rs}(709)/R_{rs}(665)$  are commonly used to relate the  
540 shape of reflectance to biogeochemical properties, notably phytoplankton absorption signals in the blue/green  
541 and near infrared/red part of the spectrum. The band ratios for each processor were evaluated against *in situ*  
542 band ratios (Fig. 9), to assess the potential for retrieving accurate spectral shapes and phytoplankton biomass  
543 in these CDOM rich waters. Owing to limited spectral variability in the dataset, the band ratios from all  
544 processors had relatively low correlations ( $R^2 < 0.36$ ) with the *in situ* observations.  $\psi$  varied from 5.7% at  
545  $R_{rs}(709)/R_{rs}(665)$  by C2R-CC to 94% at  $R_{rs}(443)/R_{rs}(560)$  using MEGS.  $R_{rs}(490)/R_{rs}(560)$  had a relatively  
546 stable accuracy compared to other band ratios with  $\psi$  of 18–31% and  $\Delta$  of 0.12–0.32 for all AC processors.  
547  $R_{rs}(490)/R_{rs}(560)$  retrieved by POLYMER had better agreement with the *in situ* values with  $\psi = 18\%$  and  $\Delta =$   
548 0.12. Compared with  $R_{rs}(443)/R_{rs}(560)$  and  $R_{rs}(490)/R_{rs}(560)$ , the retrieval accuracy for  $R_{rs}(709)/R_{rs}(665)$  was  
549 better with low  $\psi$  and  $\Delta$  of 10.2% and 0.08 for CC, 13.8% and 0.1 for C2R-Lakes, 5.7% and 0.05 for C2R-CC,  
550 17.7% and 0.14 for FUB, and 12.5% and 0.11 for MEGS. This suggests that the best retrieval of spectral shape  
551 occurs in the red to NIR domain.

552



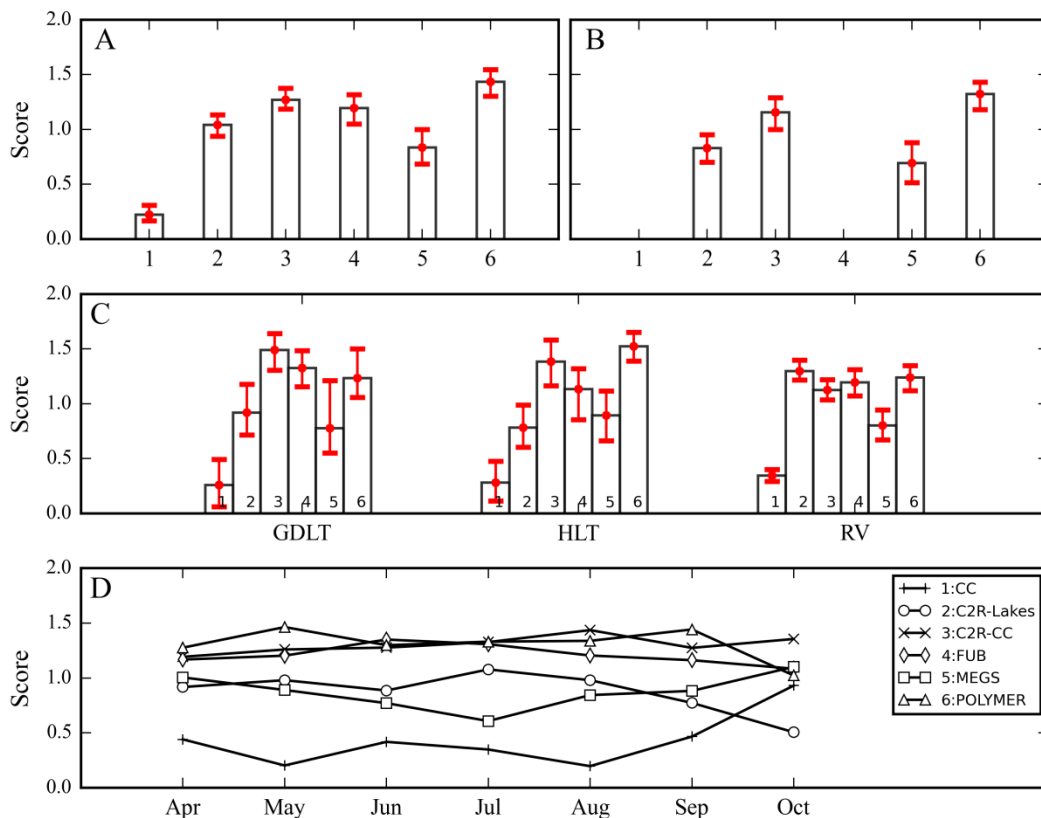
553  
 554 Fig. 9. Scatter plots of band ratio between MERIS-derived and *in situ*  $R_{rs}$ . Markers and symbols are as described for Fig. 3.  
 555

556 3.6. Statistical ranking of the accuracy of AC processors

557 Based on the statistical metrics given in Figs. 3–8 and Table 5 for all match-up data, the ranked scores of

558 all processors is given in Fig. 10A and the subset of match-ups shared between C2R-Lakes, C2R-CC, MEGS  
 559 and POLYMER is given in Fig. 10B.

560



561 Fig. 10. Scores assigned to the  $R_{rs}$  retrieval performance of each processor (1. CC; 2. C2R-Lakes; 3. C2R-CC; 4. FUB; 5. MEGS;  
 562 6. POLYMER). (A) Scores when including all data available for each processor. (B) Scores obtained with observations shared  
 563 between C2R-Lakes, C2R-CC, MEGS, and POLYMER. (C) Scores (all data and processors included) separated by data source  
 564 (GDLT = Gustaf Dalen Lighthouse Tower, HLT = Helsinki Lighthouse Tower, RV = Research Vessel). (D) Scores separated by  
 565 month. Error bars in panels A-C are the 2.5% and 97.5% confidence interval of the scores (see text).  
 566

567

568 For each processor, POLYMER showed the highest score of 1.43 and a 95% confidence interval of 1.31  
 569 to 1.55. C2R-CC and FUB had the next highest scores (1.18–1.37 and 1.05–1.32, respectively), and the  
 570 overlapping error bars between them indicated statistical similarity (Fig. 10A). CC had the lowest score (~  
 571 0.22), indicating that it was the least accurate processor.

572 For shared observations, the performance of C2R-Lakes, C2R-CC, MEGS and POLYMER was similar to  
 573 those for all processors using all match-ups. POLYMER still obtained the highest score (~ 1.32 with a 1.19–  
 574 1.44 at 95 % confidence interval), followed by C2R-CC (~ 1.15; 1.00–1.29), and MEGS with a score of 0.69.

575 Further comparisons of these ranked scores to account for differences between methods (Shipborne vs

576 AERONET\_OC), locations (coastal AERONET-OC and open Baltic Sea) and months are given in Fig. 10C &  
577 D. For the GDLT, C2R-CC had the highest score (~ 1.49; 1.31–1.65 at 95 % confidence; Fig. 10C), followed  
578 by FUB and POLYMER with the average scores of 1.33 and 1.23, respectively. For the HLT, the highest score  
579 was obtained for POLYMER (~ 1.52), followed by C2R-CC (~ 1.38). For the shipborne observations,  
580 C2R-Lakes and POLYMER had similar mean scores (~ 1.27; 1.12–1.40 at 95% confidence). C2R-CC and  
581 FUB exhibited slightly lower scores of about 1.15, and CC had consistently the lowest score (~ 0.35).

582 The monthly scores of each processor are shown in Fig. 10 D based on the match-ups between MERIS  
583 and AERONET-OC observations. The ranges of the average scores separated by month are 0.19–0.94 for CC,  
584 0.50–1.08 for C2R-Lakes, 1.09–1.35 for FUB, 0.61–1.11 for MEGS, 1.02–1.46 for POLYMER and 1.19–1.43  
585 for C2R-CC. The scores of POLYMER, C2R-CC and FUB were consistently > 1.0, indicating better than  
586 average performance throughout the seasons. C2R-Lakes scored highest in July (~1.07), and CC always scored  
587 lowest.

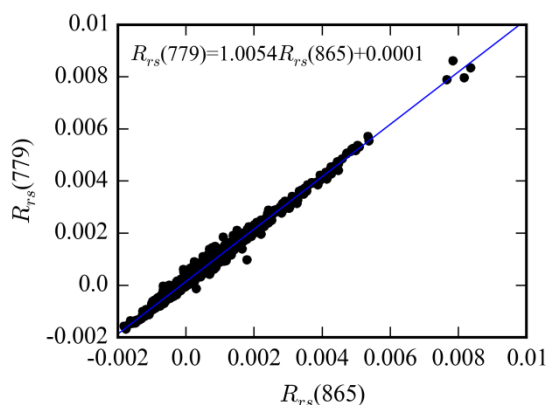
588

## 589 4. Discussion

### 590 4.1. Offset correction for shipborne observations

591 Shipborne  $R_{rs}$  in 750–900 nm bands was high compared to previous observations in the Baltic Sea (Ficek  
592 *et al*, 2011). The sources of these differences were investigated. The NIR spectrum is largely determined by  
593 the absorption of pure water except in optically turbid waters, in which case NIR reflectance ratios approach  
594 constant values, a phenomenon known as the ‘NIR similarity spectrum’ (Ruddick *et al*, 2006). The shipborne  
595 observations (before offset correction) showed a linear regression between  $R_{rs}(779)$  and  $R_{rs}(865)$  of  
596  $R_{rs}(779)=1.0054R_{rs}(865)+0.0001$  with a high correlation ( $R^2=0.99$ ; Fig. 11) and slope near unity. For the turbid  
597 waters of the North Sea it has been reported that this value should approach 1.82 (Ruddick *et al*, 2006). This  
598 suggests that the NIR signal of the Baltic Sea shipborne observations does not represent significant particle  
599 scattering as no discernable variation due to the absorption characteristics of pure water are observed. The high  
600 reflectance from 750–900 nm in the Baltic Sea is therefore likely caused by residual effects of surface  
601 contamination effects from waves, ship movement, spray, or whitecaps. It may be assumed that this effect is  
602 spectrally neutral because the fingerprint method (Simis and Olsson 2013) already accounts for the combined  
603 effect of diffuse and specular reflection at the water surface. Sun glint effects are likely minor due to the use of  
604 a sun-tracking platform measuring water-leaving radiance at an azimuth angle close to 135° from the solar  
605 azimuth. Nevertheless, due to the low amplitude of water-leaving radiance in the highly absorbing waters of

606 the Baltic Sea, the residual offset can become significant with respect to the amplitude of reflectance. It is  
 607 likely that a similar correction is not needed in more turbid water bodies. Since the AERONET-OC  
 608 observations are made from a fixed platform, they are less prone to sea spray, tilt and roll that can affect the  
 609 shipborne observations, hence there is no or little residual offset in these data. Following offset correction, the  
 610 shipborne reflectance spectra and AERONET-OC observation produced a continuous pattern compared to the  
 611 MERIS-derived reflectance bands.  
 612



613  
 614 Fig. 11. Relationship between  $R_{rs}(779)$  and  $R_{rs}(865)$  in shipborne observations.  
 615

#### 616 4.2. Match-up time window

617 The time window between *in situ* collection and satellite overpass was a compromise between reducing  
 618 the effects of temporal variability in the *in situ* data and obtaining a large volume of match-up observations. It  
 619 has been recommended to restrict match-up windows to  $\pm 3$  h in Case 1 waters and no more than  $\pm 0.5$  h in Case  
 620 2 waters (Bailey & Werdell, 2006). However, the movement of water masses, rate of vertical mixing, and the  
 621 motility of phytoplankton ultimately determine how fast optical conditions change. Tidal currents in the Baltic  
 622 Sea are slight due to limited connectivity with the Atlantic Ocean in the Baltic. The movement of water masses  
 623 in the Baltic Sea resembles a quasi-enclosed estuary supplied with fresh water from river runoff. The basins  
 624 are normally well-mixed within the visible surface layer, except during some phytoplankton bloom periods  
 625 (Drozdowska, 2007). Comparison results within various time windows ( $\pm 0.5$ –12 h) between the shipborne  
 626 observations and MERIS over-pass suggest that a  $\pm 3$ -h window yielded a useful number of match-ups and  
 627 close to optimal statistical match-up performance.  
 628

### 629 4.3. Accuracy assessment of AC processors

630 Our results showed a variable number of match-ups between the six AC processors. For the neural  
631 network based processors, the numbers were dependent on the range of the training datasets. CC developed for  
632 Case 2 waters had the lowest number of match-up pairs, indicated that more pixels retrieved by CC were out of  
633 the training range and the range of CC was not available to the Baltic Sea. C2R-CC, in contrast, showed the  
634 largest number of match-ups due to the increased range in the training dataset of the neural network.  
635 POLYMER also obtained a higher number of match-ups as it applies less stringent flagging of the processor  
636 output.

637 The radiometric validation results illustrated that the six AC processors had the lowest accuracy at shorter  
638 wavebands (412 and 443 nm). The accuracies improved from 490 to 560 nm, but the deviations increased  
639 again at longer wavebands ( $> 709$  nm), corresponding to varying amplitude of Baltic Sea reflectance between  
640 these bands, which are similar to previous studies (Beltrán-Abaunza *et al.*, 2014; Attila *et al.* 2013; Zibordi  
641 *et al.*, 2009a; Zibordi *et al.*, 2013). Based on the AERONET-OC data collected at the HLT and GDLT stations,  
642 Zibordi *et al.* (2013) found that MERIS  $L_{WN}$  by MEGS at the 490, 560 and 665 nm bands had lower deviation  
643 ( $\psi < 24\%$ ) and moderate correlation ( $R^2 > 0.39$ ) than the blue bands (412 and 443 nm). Beltrán-Abaunza *et al.*  
644 (2014) used the in-water radiometer to compare the MERIS  $\rho_w(\lambda)$  obtained by the MEGS, C2R and FUB  
645 processors on the Northern Baltic Proper. Better consistency with *in situ* observations was found at 560 nm  
646 with the correlation coefficient of 0.91 for MEGS, 0.87 for C2R and 0.84 for FUB, and the worst consistency  
647 was at 412 nm for these three processors. The relatively weak  $R_{rs}$  at blue bands (412 and 443 nm) is  
648 characteristic of the optical properties of highly absorbing waters. The contribution of the reflectance at the sea  
649 surface to the top-of-atmospheric radiance is therefore low, which amplifies the errors at these wavebands.  
650 This resulted in the poor performance to retrieve  $R_{rs}$  in the blue wavebands.

651 The combined validation results assigned the POLYMER processor the highest overall score, better  
652 correlation, lowest deviations and highest number of match-ups compared against all other processors. This  
653 indicated that POLYMER was the most accurate processor applied to MERIS for the Baltic Sea. Owing to the  
654 flexibility of this model, POLYMER exhibited the smallest deviation and highest score in the Case 1 and Case  
655 2 waters compared to MEGS, SeaDAS and Forward NN (Müller *et al.*, 2015). POLYMER also showed the best  
656 performance and highest score in the CDOM dominated waters of the Baltic Sea, throughout the observation  
657 period. Even so, the accuracy of retrieval at blue wavelengths was worse than at longer wavelengths for  
658 POLYMER and this still requires improvement. Possible reasons for this were that the absorption of CDOM

659 was neglected or expressed as the Chl *a* concentration in the bio-optical model. In the Baltic Sea CDOM does  
660 not co-vary with Chl *a* and significantly affects the blue to green range of the spectra.

661 Among the four neural network AC processors (CC, C2R-Lakes, C2R-CC and FUB), C2R-CC showed  
662 the best performance and CC the worst, which is likely to be due to the training data sets used to calibrate the  
663 neural network. This calibration also includes the effects of different aerosol types, cirrus clouds, sun and sky  
664 radiance, and the coupling between them and the air molecules. The atmospheric masses in the Baltic Sea are  
665 affected by both land and marine due to its geographical position. The average aerosol optical thickness was  
666 about 1.3 as determined at the island of Gotland in the central part of the basin (Carlund *et al.*, 2005). The  
667 higher values of the aerosol optical thickness over the Baltic Sea in April may be related to the burning of  
668 agricultural waste straw in northern Europe and Russia (Zdun *et al.*, 2011). The standard AC used in CC was  
669 not suited to this region, which resulted in the worst performance of all the processors tested. The mixture of  
670 maritime and continental aerosol models may account for the improved accuracy of FUB and C2R-Lakes. The  
671 coastal aerosol model used in C2R-CC is appropriate for the Baltic Sea. The maximum CDOM absorption  
672 used to generate the simulated reflectance in the training databases was  $1 \text{ m}^{-1}$  at 443nm for CC, C2R-Lakes,  
673 C2R-CC and FUB, which was sufficient for most areas of the Baltic Sea except for areas near large rivers in  
674 the north and east which are not close to the AERONET-OC or shipborne stations.

675 The performance of MEGS 8.1 was poor in the Baltic Sea, most likely because it was primarily designed  
676 for open ocean waters dominated by phytoplankton, but it uses the bright pixel (BP) AC in highly scattering  
677 waters. In the Baltic Sea however, the BPAC is rarely triggered and only the open ocean AC model is used in  
678 this region. The constant for  $R_{rs}(510)$  was obtained from the Case 1 waters, and likely resulted in larger  
679 derivations from the actual aerosol and path radiance when used in high-CDOM absorption waters of the  
680 Baltic Sea. An over-correction of the atmospheric signal resulted in the bias ( $\delta$ ) being less than zero at blue and  
681 green wavebands (Fig. 7).

682 The use of such a comprehensive data set for the Baltic Sea has wider implications for other similar high  
683 CDOM waters and for the new generation of Copernicus Sentinels, which additionally have short wave infra-red  
684 (SWIR) bands that can potentially improve the performance of AC models (Wang *et al.* 2007). The estuaries of  
685 the Northern most parts of the Gulf of Bothnia, in Finland and Sweden, and the Eastern most part of the Gulf  
686 of Finland are the highest absorbing CDOM waters in the region (Kowalczyk *et al.*, 1999; Ylöstalo *et al.*,  
687 2016), but were not covered by the shipborne observations.

688

689 4.4 Implications for use of AC processors with band ratio algorithms

690 The retrieval of biogeochemical components, such as the Chl *a* concentration, from satellite sensors  
691 depends on the availability of suitable algorithms, as well as the performance of atmospheric correction to  
692 accurately retrieve both the amplitude and shape of  $R_{rs}$  at the sea surface from the TOA radiances. Band ratio  
693 algorithms are common in optically complex and productive waters, and can reduce systematic retrieval error  
694 caused by atmospheric corrections when the aerosols are not absorbing, i.e. when the error affects the bands  
695 used in the band ratio in equal measure. Low correlation coefficients between satellite and *in situ* reflectance  
696 band ratios appear to have been caused by a highly conserved shape of the  $R_{rs}$  spectrum in the Baltic Sea  
697 resulting in a narrow range of band ratio values.

698 For all six atmospheric correction processors, the bias between MERIS and *in situ* observations at blue  
699 wavebands was larger than at blue-green bands, which resulted in poor retrieval of  $R_{rs}(443)/R_{rs}(560)$  ratios (Fig.  
700 9) suggesting that these band ratios are not suitable to retrieve biogeochemical products in these waters. For  
701 POLYMER, the MERIS-retrieved  $R_{rs}(490)/R_{rs}(560)$  had the best agreement with the *in situ* data. The retrieval  
702 of  $R_{rs}(709)/R_{rs}(665)$  ratios improved for some processors, such as C2R-CC, C2R-Lakes, CC, FUB and MEGS  
703 which is relevant for retrieving Chl *a* in highly absorbing waters when the use of blue-green ratios can be  
704 erroneous.

705 For all processors, the blue-green ratio of  $R_{rs}(443)/R_{rs}(560)$  exhibitdd the worst performance with the  
706 lowest  $R^2$  ( $< 0.11$ ) and largest  $\psi$  (38.1–72.5%).  $R_{rs}$  is low in the blue region due to the high absorption by  
707 CDOM, and the performance of  $R_{rs}(490)/R_{rs}(560)$  ratios were better compared to  $R_{rs}(443)/R_{rs}(560)$  ratios since  
708 the  $R_{rs}(490)$  signal was stronger than  $R_{rs}(443)$ , which may be relevant for Chl *a* algorithms such as OC3 and  
709 OC4 when they use the  $R_{rs}(490)/R_{rs}(560)$  ratios. Pitarch *et al.* (2016), however used the regional calibration of  
710 OC4v6 to map the Chl *a* concentration in the Baltic Sea, but they found that OC4v6 over-estimates Chl *a*  
711 resulting in a  $R^2 = 0.43$  and bias of 0.44, suggesting that Chl *a* algorithms for the Baltic Sea, should use longer  
712 wavelengths than  $R_{rs}(490)$ . In their analysis, they also included data from the Kattegat and Skagerrak which  
713 proved to be more accurate with blue : green Chl *a* algorithms than for the Baltic Sea area. Considering that  
714 600 nm was the waveband for minimum particle absorption and that pigment absorption dominated the total  
715 absorption at wavelengths longer than 510 nm, Darecki *et al.* (2003) shifted the wavelengths from  
716  $R_{rs}(490)/R_{rs}(550)$  to  $R_{rs}(550)/R_{rs}(590)$  in empirical Chl *a* algorithm. Better results were obtained with  $R^2 = 0.75$   
717 and  $\psi = 20\%$ . Based solely on our observations of the radiometric retrieval accuracy of AC models, other Chl  
718 *a* algorithms, including NIR-red ratio algorithms and possibly algorithms based on fluorescence line height,

719 could improve the accuracy of Chl *a* retrieval..

720 The band ratio  $R_{rs}(709)/R_{rs}(665)$  showed the highest accuracy for C2R-CC and C2R-Lakes. Ligi *et al*  
721 (2016) recently showed, that the NIR-Red model  $R_{rs}(709)/R_{rs}(665)$  is most suitable for Chl *a* concentration  
722 based on a large dataset of simulated  $R_{rs}(\lambda)$  and field measurements in the Baltic Sea. The wavelength region  
723 from 620 nm to 709 nm provides essential features for Chl *a* estimation, as well as absorption diagnostic of  
724 cyanobacteria pigments at 620 nm, smaller interference of CDOM absorption, and the light scattering peak  
725 near 709 nm where absorption of water constituents is small with respect to absorption by water. Accurate  
726 retrieval of  $R_{rs}$  in the NIR-red region in general and the  $R_{rs}(709)/R_{rs}(665)$  ratio in particular should therefore be  
727 considered a priority in further AC and in-water algorithm validation. Currently, three AC processors  
728 (POLYMER, C2R-CC and C2R-Lakes) exhibit promising results in this spectral domain.

729

730 The 709 nm band as well as retrieval further into the NIR also plays an essential role in the detection of  
731 surface accumulation of phytoplankton, such as cyanobacteria blooms in the Baltic Sea during calm weather in  
732 summer (Groetsch et al. 2014). During the field campaigns only small surface blooms were encountered and  
733 few co-occured during clear-sky satellite passes, so we can only focus on the systematic  $R_{rs}$  retrieval  
734 performance of the various AC schemes during relatively well mixed conditions. Reflectance retrieval over  
735 patchy, sub-pixel sized surface blooms is an enormous challenge both from the perspective of satellite AC and  
736 *in situ* data collection. Neither the AERONET (due to its limited band set) nor the shipborne (disturbance of  
737 the water mass) platforms are well suited to perform this matchup analysis. Spectra characteristic of surface  
738 blooms were therefore not included in this analysis.

739

## 740 5 Conclusions

741 The performance of six AC processors (CC, C2R-Lakes, C2R-CC, FUB, MEGS, and POLYMER) for  
742 MERIS was assessed in the Baltic Sea, against *in situ* remote sensing reflectance from AERONET-OC and  
743 shipborne measurements. All six processors showed poor performances in the blue (412 and 443 nm) and NIR  
744 wavebands (754–865 nm), but better performances at 490 to 709 nm except for CC. The CC processor  
745 exhibited the worst accuracy with  $\psi > 190\%$  for all wavebands. POLYMER exhibited the best performance at  
746 MERIS bands from 490–709 nm and had the lowest deviations ( $\psi = 12\text{--}29\%$ ) and bias ( $\delta = -0.3\text{--}0.1$ ) and the  
747 highest correlation ( $R^2 = 0.66\text{--}0.91$ ) when compared to the *in situ* data. C2R-CC was the second most accurate  
748 algorithm. The retrieval of  $R_{rs}(709)/R_{rs}(665)$  was supported by all processors, suggesting that accurate Chl *a*

749 concentrations for the Baltic Sea are feasible. Further improvement in POLYMER and C2R-CC at blue and  
750 NIR bands, which are both still under development, would improve their applicability for highly absorbing  
751 waters such as the Baltic Sea.

752 This analysis represents the largest data set used to date to test a range of AC models for the highly  
753 absorbing waters of the Baltic Sea, and is therefore relevant and applicable to other highly absorbing water  
754 bodies such as the Arctic Ocean, The Yellow Sea, the Black Sea, the River mouths of the Amazon and a large  
755 range of freshwater lakes, where ocean colour products still prove to be erroneous.

756

## 757 Acknowledgements

758 SS and GT were funded by the European Space Agency SEOM contract Extreme Case 2 waters (C2X)  
759 (4000113691/15/I-LG). PQ was funded by a scholarship from the Chinese Scholarship Program. We thank the  
760 crew of RV *Aranda* and colleagues from the Finnish Environment Institute (SYKE) for the data collected  
761 during research cruises. We are grateful to Giuseppe Zibordi from the Joint Research Center for  
762 AERONET-OC data from the Gustaf Dalen and Helsinki Lighthouse Tower and for valuable comments on a  
763 draft of the manuscript.

764

## 765 References

- 766 Aiken, J., & Moore, G. (2000). Case 2 (S) bright pixel atmospheric correction. MERIS ATBD, 2,6-6.  
767 Antoine, D., & Morel, A. (2011). Atmospheric correction of the MERIS observations over ocean Case 1 waters.  
768 Tech. rep., MERIS ATBD 2.7, issue 5, revision 5. [http://envisat.esa.int/instruments/meris/atbd/atbd\\_2.7.pdf](http://envisat.esa.int/instruments/meris/atbd/atbd_2.7.pdf).  
769 Attila, J., Koponen, S., Kallio, K., *et al.* (2013). MERIS Case II water processor comparison on coastal sites of the  
770 northern Baltic Sea. *Remote sensing of environment*, 128, 138-149.  
771 Aznay, O., & Santer, R. (2009). MERIS atmospheric correction over coastal waters: validation of the MERIS  
772 aerosol models using AERONET. *International Journal of Remote Sensing*, 30(18), 4663-4684.  
773 Bailey, S. W., & Werdell, P. J. (2006). A multi-sensor approach for the on-orbit validation of ocean color satellite  
774 data products. *Remote Sensing of Environment*, 102(1), 12-23.  
775 Beltrán-Abaunza, J. M., Kratzer, S., & Brockmann, C. (2014). Evaluation of MERIS products from Baltic Sea  
776 coastal waters rich in CDOM. *Ocean Science*, 10(3), 377-396.  
777 Brewin, R. J., Sathyendranath, S., Müller, D., *et al.* (2015). The Ocean Colour Climate Change Initiative: III. A  
778 round-robin comparison on in-water bio-optical algorithms. *Remote Sensing of Environment*, 162, 271-294.  
779 Brockmann, C., Doerffer, R., Peters, M., *et al.* (2016). Evolution of the C2R-CC neural network for Sentinel 1 and  
780 3 for the retrieval of ocean colour products in normal and extreme optically complex waters, In Proceedings  
781 ESA Living Planet Symposium Prague, 09-13, May.  
782 Callieco, F., & Dell'Acqua, F. (2011). A comparison between two radiative transfer models for atmospheric  
783 correction over a wide range of wavelengths. *International Journal of Remote Sensing*, 32(5), 1357-1370.  
784 Carlund, T., Håkansson, B., & Land, P. (2005). Aerosol optical depth over the Baltic Sea derived from AERONET

785 and SeaWiFS measurements. *International Journal of Remote Sensing*, 26(2), 233-245.

786 D'Alimonte, D., Zibordi, G., Berthon, J-F., Canuti, E., Kajiyama, T. (2012) Performance and applicability of  
787 bio-optical algorithms in different European seas. *Remote Sensing of Environment*, 124: 402-412.

788 Darecki, M., Weeks, A., Sagan, S., Kowalczyk, P., & Kaczmarek, S. (2003). Optical characteristics of two  
789 contrasting Case 2 waters and their influence on remote sensing algorithms. *Continental Shelf Research*, 23(3),  
790 237-250.

791 Darecki, M., & Stramski, D. (2004). An evaluation of MODIS and SeaWiFS bio-optical algorithms in the Baltic Sea.  
792 *Remote Sensing of Environment*, 89(3), 326-350.

793 Doerffer, R., & Schiller, H. (2007). The MERIS Case 2 water algorithm. *International Journal of Remote Sensing*,  
794 28(3-4), 517-535.

795 Doerffer, R., Schiller, H. (2008). MERIS regional, coastal and lake case 2 water project - atmospheric correction  
796 ATBD. GKSS Research Center, Geesthacht, Germany, version 1.0, 18 May 2008.

797 Doron, M., Babin, M., Hembise, O., et al. (2011) Ocean transparency from space: Validation of algorithms using  
798 MERIS, MODIS and SeaWiFS data. *Remote Sensing of Environment*, 115: 2986-3001.

799 Drozdowska, V. (2007). Seasonal and spatial variability of surface seawater fluorescence properties in the Baltic and  
800 Nordic Seas: results of lidar experiments. *Oceanologia*, 49(1), 59-69.

801 Ficek, D., Zapadka, T., & Dera, J. (2011). Remote sensing reflectance of Pomeranian lakes and the Baltic.  
802 *Oceanologia*, 53(4), 959-970.

803 Glover, D.M., Jenkins, W. J., Doney, S.C. (2011). *Modeling methods for marine science*: Cambridge University  
804 Press.

805 Gordon, H. R., & Wang, M. (1994). Retrieval of water-leaving radiance and aerosol optical thickness over the  
806 oceans with SeaWiFS: a preliminary algorithm. *Applied optics*, 33(3), 443-452.

807 Groetsch, P. M., Simis, S. G., Eleveld, M. A., & Peters, S. W. (2014). Cyanobacterial bloom detection based on  
808 coherence between ferrybox observations. *Journal of Marine Systems*, 140, 50-58.

809 Harvey, E. T., Kratzer, S., Philipson, P. (2015) Satellite-based water quality monitoring for improved spatial and  
810 temporal retrieval of chlorophyll-a in coastal waters. *Remote Sensing of Environment*, 158: 417-430.

811 He, X., Bai, Y., Pan, D., Tang, J., & Wang, D. (2012). Atmospheric correction of satellite ocean color imagery using  
812 the ultraviolet wavelength for highly turbid waters. *Optics express*, 20(18), 20754-20770.

813 Hooker, S. B., Lazin, G., Zibordi, G., & McLean, S. (2002). An evaluation of above-and in-water methods for  
814 determining water-leaving radiances. *Journal of Atmospheric and Oceanic Technology*, 19(4), 486-515.

815 Hu, C., Carder, K. L., & Muller-Karger, F. E. (2000). Atmospheric correction of SeaWiFS imagery over turbid  
816 coastal waters: a practical method. *Remote sensing of Environment*, 74(2), 195-206.

817 IOCCG (2000), Remote sensing of ocean colour in coastal, and other optically-complex, waters, In S.  
818 Sathyendranath (Ed.), Technical report: Reports of the International Ocean-Colour Coordinating Group, No. 10,  
819 Dartmouth, Canada: IOCCG.

820 IOCCG (2010). Atmospheric Correction for Remotely-Sensed Ocean-Colour Products. In M. Wang (Ed.), Technical  
821 report: Reports of the International Ocean-Colour Coordinating Group, No. 10, Dartmouth, Canada: IOCCG.

822 Kahru, M., Elmgren, R., & Savchuk, O. P. (2015). Changing seasonality of the Baltic Sea. *Biogeosciences*  
823 *Discussions*, 12(22), 18855-18882.

824 Knaeps, E., Dogliotti, A. I., Raymaekers, D., Ruddick, K., & Sterckx, S. (2012). *In situ* evidence of non-zero  
825 reflectance in the OLCI 1020nm band for a turbid estuary. *Remote Sensing of Environment*, 120,  
826 133-144. Kratzer, S., Brockmann, C., Moore, G. (2008) Using MERIS full resolution data to monitor coastal  
827 waters - A case study from Himmerfjorden, a fjord-like bay in the north western Baltic Sea. *Remote Sensing of*  
828 *Environment*, 112: 2284-2300.

829 Koponen, S., Attila, J., Pulliainen, J., Kallio, K., Pyhälähti, T., Lindfors, A., Rasmus, K., & Hallikainen, M.  
830 (2007). A case study of airborne and satellite remote sensing of a spring bloom event in the Gulf of  
831 Finland. *Continental Shelf Research*, 27(2), 228-244.

832 Kowalczyk, P. (1999). Seasonal variability of yellow substance absorption in the surface layer of the Baltic Sea.  
833 *Journal of Geophysical Research-Oceans*, 104, C12, 30047-30058.

834 Krawczyk, H., Neumann, A., Walzel, T., Hetscher, M., Siegel, H. (1997). Application of multispectral interpretation  
835 algorithm to remote sensing data over the Baltic Sea. *Ocean Optics XIII, Proceedings of the Society of*  
836 *Photo-optical Instrumentation Engineers (SPIE)*. 2963: 234-239.

837 Lenoble, J., Herman, M., Deuzé, J. L., Lafrance, B., Santer, R., & Tanré, D. (2007). A successive order of scattering  
838 code for solving the vector equation of transfer in the earth's atmosphere with aerosols. *Journal of Quantitative*  
839 *Spectroscopy and Radiative Transfer*, 107(3), 479-507.

840 Leppäranta, M., & Myrberg, K. (2009). *Physical oceanography of the Baltic Sea*. Springer Science & Business  
841 Media.

842 Ligi, M., Kutser, T., Kallio, K., *et al.* (2016). Testing the performance of empirical remote sensing algorithms in the  
843 Baltic Sea waters with modelled and *in situ* reflectance data. *Oceanologia*.

844 Matthews, M.W. (2011). A current review of empirical procedures of remote sensing in inland and near coastal  
845 transitional waters. *International Journal of Remote Sensing*, 32(21), 6855-6899.

846 Melin, F., Zibordi, G., Berthon, J-F. (2007) Assessment of satellite ocean color products at a coastal site. *Remote*  
847 *Sensing of Environment*, 110: 192-215.

848 Moore, G. F., & Lavender, S. (2011). MERIS ATBD 2.6. Case II. S Bright Pixel Atmospheric Correction. URL.  
849 [https://earth.esa.int/documents/700255/2042855/MERIS\\_ATBD\\_2.6\\_v5.0+-+2011.pdf](https://earth.esa.int/documents/700255/2042855/MERIS_ATBD_2.6_v5.0+-+2011.pdf)

850 Mobley, C. D. (1999). Estimation of the remote-sensing reflectance from above-surface measurements. *Applied*  
851 *Optics*, 38(36), 7442-7455.

852 Mobley, C. D. (2015). Polarized reflectance and transmittance properties of windblown sea surfaces. *Applied optics*,  
853 54(15), 4828-4849.

854 Müller, D., Krasemann, H., Brewin, R. J., *et al.* (2015). The Ocean Colour Climate Change Initiative: I. A  
855 methodology for assessing atmospheric correction processors based on in-situ measurements. *Remote Sensing*  
856 *of Environment*, 162, 242-256.

857 Nobileau, D., & Antoine, D. (2005). Detection of blue-absorbing aerosols using near infrared and visible (ocean  
858 color) remote sensing observations. *Remote Sensing of Environment*, 95(3), 368-387.

859 Ohde, T; Sturm, B; Siegel, H. (2002) Derivation of SeaWiFS vicarious calibration coefficients using in situ measurements in Case 2 water  
860 of the Baltic Sea. *Remote Sensing of Environment*, 80: 248-255.

861 Omstedt, A., Elken, J., Lehmann, A., & Piechura, J. (2004). Knowledge of the Baltic Sea physics gained during the  
862 BALTEX and related programmes. *Progress in Oceanography*, 63(1), 1-28.

863 Pierson, D. C., Kratzer, S., Strombeck, N. (2008) Relationship between the attenuation of downwelling irradiance at  
864 490 nm with the attenuation of PAR (400 nm-700 nm) in the Baltic Sea. *Remote Sensing of Environment*, 112:  
865 668-680.

866 Pitarch, J., Volpe, G., Colella, S., Krasemann, H., & Santoleri, R. (2016). Remote sensing of chlorophyll in the  
867 Baltic Sea at basin scale from 1997 to 2012 using merged multi-sensor data. *Ocean Science*, 12(2), 379-389.

868 Reinart, A., Kutser, T. (2006) Comparison of different satellite sensors in detecting cyanobacterial bloom events in  
869 the Baltic Sea. *Remote Sensing of Environment*, 102: 74-85.

870 Robert, C., & Casella, G. (2013). *Monte Carlo statistical methods*. Springer Science & Business Media.

871 Ruddick, K. G., Ovidio, F., & Rijkeboer, M. (2000). Atmospheric correction of SeaWiFS imagery for turbid coastal  
872 and inland waters. *Applied optics*, 39(6), 897-912.

873 Ruddick, K. G., De Cauwer, V., Park, Y. J., & Moore, G. (2006). Seaborne measurements of near infrared

874 water-leaving reflectance: The similarity spectrum for turbid waters, *Limnol. Oceanogr.*, 51(2), 1167–1179.

875 Schiller, H., & Doerffer, R. (1999). Neural network for emulation of an inverse model operational derivation of  
876 Case II water properties from MERIS data. *International journal of remote sensing*, 20(9), 1735-1746.

877 Schroeder, T., Schaale, M., & Fischer, J. (2007). Retrieval of atmospheric and oceanic properties from MERIS  
878 measurements: A new Case 2 water processor for BEAM. *International Journal of Remote Sensing*, 28(24),  
879 5627-5632.

880 Siegel, D. A., Wang, M., Maritorena, S., & Robinson, W. (2000). Atmospheric correction of satellite ocean color  
881 imagery: the black pixel assumption. *Applied optics*, 39(21), 3582-3591.

882 Simis, S. G. H., & Olsson, J. (2013). Unattended processing of shipborne hyperspectral reflectance measurements.  
883 *Remote Sensing of Environment*, 135, 202-212.

884 Steinmetz, F., Deschamps, P.Y., & Ramon, D. (2011). POLYMER--Atmospheric correction in presence of sun glint:  
885 application to MERIS. *Opt Express*, 19(10), 9783-9800.

886 Stramska, M., Swirgon, M. (2014) Influence of atmospheric forcing and freshwater discharge on interannual  
887 variability of the vertical diffuse attenuation coefficient at 490 nm in the Baltic Sea. *Remote Sensing of*  
888 *Environment*, 40: 155-164.

889 Thuillier, G., Hersé, M., Foujols, T., *et al.* (2003). The solar spectral irradiance from 200 to 2400 nm as measured by  
890 the SOLSPEC spectrometer from the ATLAS and EURECA missions. *Solar Physics*, 214(1), 1-22. Voss, K. J.,  
891 Morel, A., Antoine, D. (2007) Detailed validation of the bidirectional effect in various Case 1 waters for  
892 application to ocean color imagery. *Biogeosciences*, 4, 781-789.

893 Wang, M., & Shi, W. (2007). The NIR-SWIR combined atmospheric correction approach for MODIS ocean color  
894 data processing. *Optics Express*, 15(24), 15722-15733.

895 Woźniak, M., Bradtke, K. M., & Krężel, A. (2014). Comparison of satellite chlorophyll a algorithms for the Baltic  
896 Sea. *Journal of Applied Remote Sensing*, 8(1), 083605.

897 Ylöstalo, P., Seppälä, J., Kaitala, S., Maunula, P., & Simis, S. (2016). Loadings of dissolved organic matter and  
898 nutrients from the Neva River into the Gulf of Finland–Biogeochemical composition and spatial distribution  
899 within the salinity gradient. *Marine Chemistry*, 186, 58-71.

900 Zibordi, G., Berthon, J. F., Mélin, F., D'Alimonte, D., & Kaitala, S. (2009a). Validation of satellite ocean color  
901 primary products at optically complex coastal sites: Northern Adriatic Sea, Northern Baltic Proper and Gulf of  
902 Finland. *Remote Sensing of Environment*, 113(12), 2574-2591.

903 Zibordi, G., Mélin, F., Berthon, J.-F., *et al.* (2009b). AERONET-OC: A Network for the Validation of Ocean Color  
904 Primary Products. *Journal of Atmospheric and Oceanic Technology*, 26(8), 1634-1651.

905 Zibordi, G., Mélin, F., Berthon, J. F., & Canuti, E. (2013). Assessment of MERIS ocean color data products for  
906 European seas. *Ocean Science*, 9(3), 521-533.

907 Zdun, A., Rozwadowska, A., & Kratzer, S. (2011). Seasonal variability in the optical properties of Baltic aerosols.  
908 *Oceanologia*, 53(1), 7-34.

909